Cell Metabolism

Article

Ketone flux through BDH1 supports metabolic remodeling of skeletal and cardiac muscles in response to intermittent time-restricted feeding

Graphical abstract

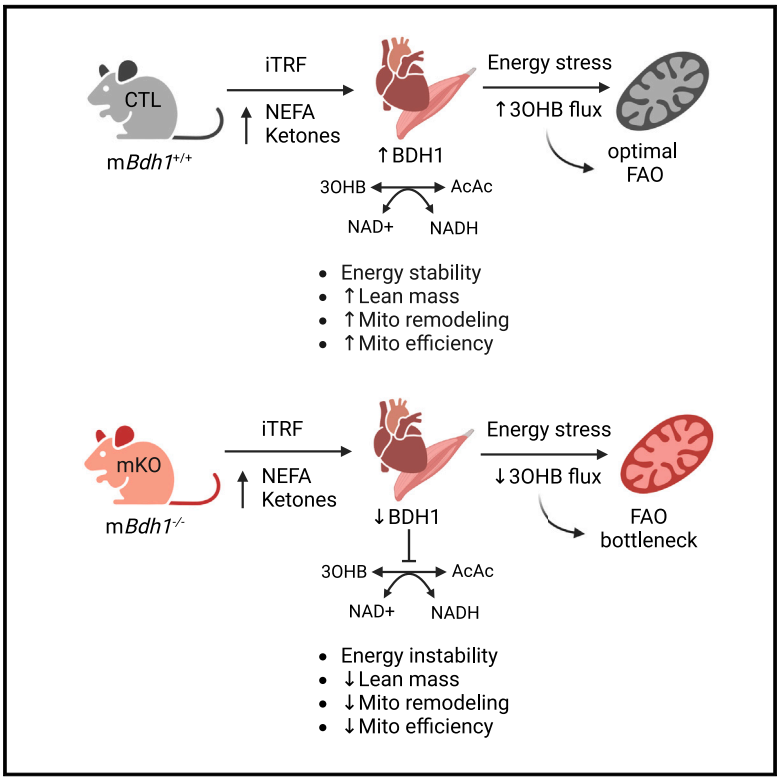

Highlights

- iTRF-induced muscle remodeling coincides with systemic adaptations in ketone flux
- Muscle ketone flux depends on fiber-type-specific mitochondrial BDH1 abundance
- BDH1 flux in striated muscles fine-tunes fat oxidation and pyruvate partitioning
- BDH1 flux in striated muscles optimizes the metabolic benefits of iTRF

Authors

Ashley S. Williams, Scott B. Crown, Scott P. Lyons, ..., Paul A. Grimsrud, Guo-Fang Zhang, Deborah M. Muoio

Correspondence

muoio@duke.edu

In brief

Researchers found that ketone flux in cardiac and skeletal muscles promotes exercise tolerance and contributes to the full adaptive benefits of an intermittent time-restricted feeding (iTRF) regimen, both attributable to an unexpected interplay between ketolysis and fat burning efficiency that occurs selectively in mitochondria residing within highly oxidative myofibers.

Williams et al., 2024, Cell Metabolism *36*, 422–437
February 6, 2024
https://doi.org/10.1016/j.cmet.2024.01.007

CellPress

CellPress

Cell Metabolism

Article

Ketone flux through BDH1 supports metabolic remodeling of skeletal and cardiac muscles in response to intermittent time-restricted feeding

Ashley S. Williams,[1,6] Scott B. Crown,[1,6] Scott P. Lyons,[1] Timothy R. Koves,[1,3] Rebecca J. Wilson,[1] Jordan M. Johnson,[1] Dorothy H. Slentz,[1] Daniel P. Kelly,[5] Paul A. Grimsrud,[1,2] Guo-Fang Zhang,[1,2] and Deborah M. Muoio[1,2,4,7,*]

[1]Duke Molecular Physiology Institute and Sarah W. Stedman Nutrition and Metabolism Center, Duke University Medical Center, Durham, NC 27701, USA

[2]Department of Medicine, Division of Endocrinology, Metabolism, and Nutrition, Duke University Medical Center, Durham, NC 27710, USA

[3]Department of Medicine, Division of Geriatrics, Duke University Medical Center, Durham, NC 27710, USA

[4]Department of Pharmacology and Cancer Biology, Duke University Medical Center, Durham, NC 27710, USA

[5]Cardiovascular Institute and Department of Medicine, Perelman School of Medicine at the University of Pennsylvania, Philadelphia, PA, USA

[6]These authors contributed equally

[7]Lead contact

*Correspondence: muoio@duke.edu

https://doi.org/10.1016/j.cmet.2024.01.007

SUMMARY

Time-restricted feeding (TRF) has gained attention as a dietary regimen that promotes metabolic health. This study questioned if the health benefits of an intermittent TRF (iTRF) schedule require ketone flux specifically in skeletal and cardiac muscles. Notably, we found that the ketolytic enzyme beta-hydroxybutyrate dehydrogenase 1 (BDH1) is uniquely enriched in isolated mitochondria derived from heart and red/oxidative skeletal muscles, which also have high capacity for fatty acid oxidation (FAO). Using mice with BDH1 deficiency in striated muscles, we discover that this enzyme optimizes FAO efficiency and exercise tolerance during acute fasting. Additionally, iTRF leads to robust molecular remodeling of muscle tissues, and muscle BDH1 flux does indeed play an essential role in conferring the full adaptive benefits of this regimen, including increased lean mass, mitochondrial hormesis, and metabolic rerouting of pyruvate. In sum, ketone flux enhances mitochondrial bioenergetics and supports iTRF-induced remodeling of skeletal muscle and heart.

INTRODUCTION

Dietary regimens encompassing various forms of intermittent fasting (IF) have been shown to confer favorable metabolic outcomes mediated by adaptations occurring in multiple organ systems. Accordingly, both IF and time-restricted feeding (TRF) are widely touted as regimens that combat obesity, enhance whole-body energy homeostasis, and extend healthspan.[1–4] Although the strongest evidence supporting the benefits of IF and TRF stems from preclinical studies in rodents and other model systems,[5–9] a growing number of human trials have likewise reported positive results.[10–16] Nonetheless, the molecular mechanisms underlying the benefits IF/TRF remain poorly understood.

Among the metabolic hallmarks of an extended fasted state is a pronounced increase in hepatic ketogenesis and the resulting rise in circulating levels of the two primary ketone bodies, beta-hydroxybutyrate (3OHB) and acetoacetate (AcAc). Ketones are well recognized as fatty acid-derived carbon fuels that are essential for the brain during periods of energy and/or carbohydrate restriction. Neurons depend on ketones when glucose supply is diminished because they have limited capacity for fatty acid oxidation (FAO).[17] By contrast, the importance of ketones in fueling skeletal muscle and heart, two tissues that have robust FAO machinery, has remained uncertain and surprisingly underexplored, particularly in the settings of TRF and IF. Also noteworthy is that ketones have gained attention as a potential cardioprotective fuel in animals and humans affected by heart failure[18,19] and are increasingly investigated for their relevance in other disease settings.[20,21] Considering mounting interest surrounding the role of ketones as an alternative fuel for cardiac and skeletal muscles, the current study sought to delineate the importance of muscle ketone flux in the contexts of acute fasting and chronic IF achieved via a newly developed intermittent TRF (iTRF) schedule. The findings show that muscle ketone metabolism is indeed required to achieve the full benefits of iTRF, attributable in part to an unexpected interplay between ketolysis and FAO efficiency that occurs selectively in mitochondria residing within highly oxidative myofibers.

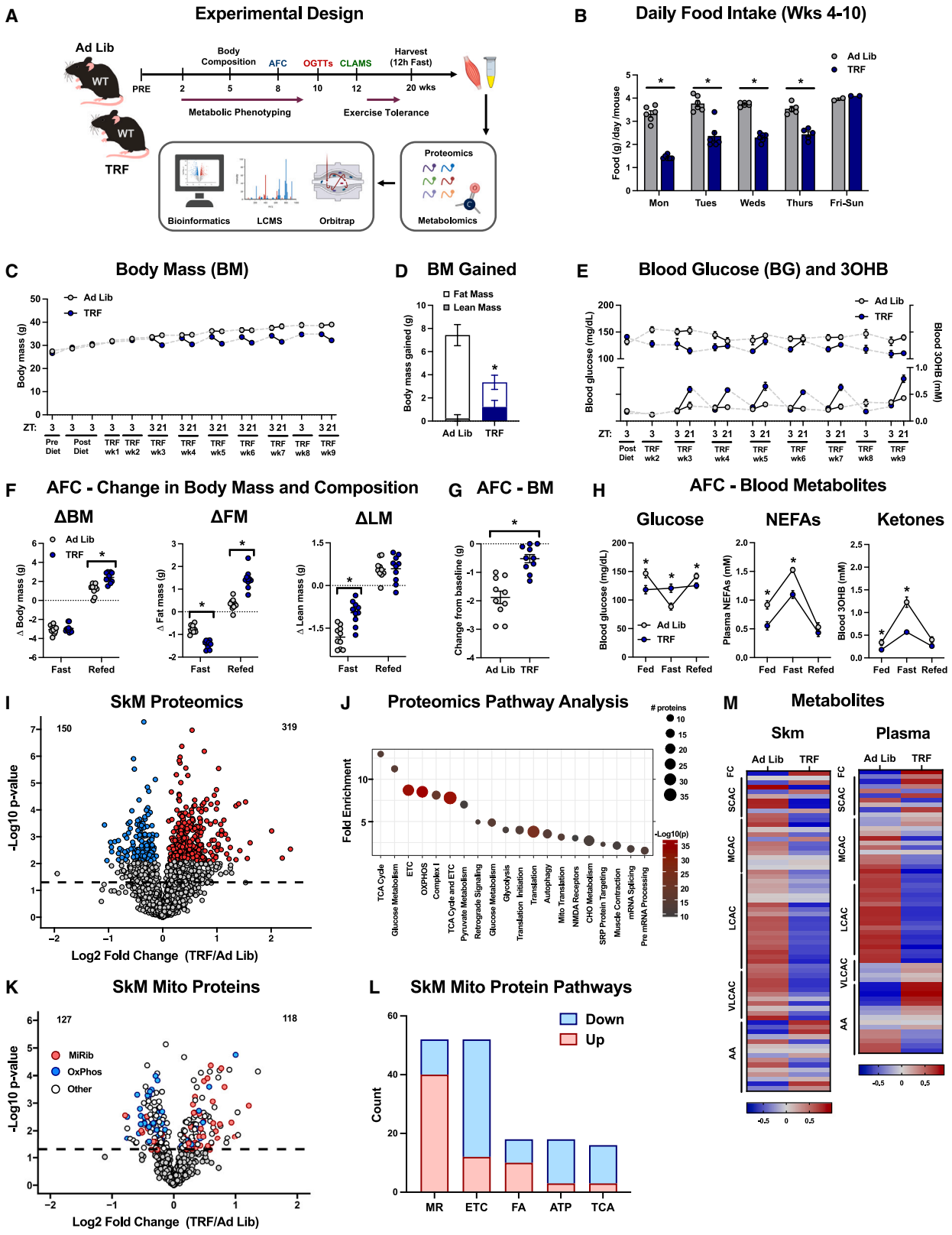

Figure 1. Intermittent TRF promotes metabolic resilience, preserves lean mass, and remodels skeletal muscle

(A) TRF experimental design.

(B) Daily food intake during TRF weeks 4–10.

(legend continued on next page)

RESULTS

Intermittent TRF promotes metabolic resilience, preserves lean mass, and remodels skeletal muscle

To advance the goals of this study, we developed an iTRF regimen (Figure 1A) wherein C57Bl/6NJ mice had access to a defined diet (Research Diets D12450Hi, 10%/17%/19% kcal as fat/sucrose/protein) for 6 h/day (zeitgeber time [ZT]21–3), four consecutive days (Monday–Thursday) per week, followed by free access to food for 3 days/week (Friday–Sunday).

This specific feeding schedule was designed based on the following rationale. First, considering growing speculation that ketones might play a key role in conferring the benefits of both TRF and IF,[4] we sought to drive a strong ketogenic response with an 18-h fasting period. Second, because 18 h of fasting is stressful for mice, we used an intermittent regimen that permitted a 3-day recovery period each week. Third, an intermittent schedule is more pragmatic and likely to be more attractive and achievable for humans than continuous TRF, and might also afford additional benefits, akin to exercise training and recovery. The regimen we employed is viewed as a hybrid between IF and TRF, which led us to use the iTRF terminology.

Animals subjected to the iTRF regimen were compared against a control group fed *ad libitum* (Ad Lib). On average, the estimated food consumption per g body mass in the iTRF group was 66% and 115% of the Ad Lib mice during Monday–Thursday and Friday–Sunday, respectively (Figure 1B), while activity levels monitored at weeks 12–13 were similar between groups (Figure S1E). Accordingly, the iTRF group consumed fewer calories and gained less total body mass and less fat mass throughout the study (Figures 1C and 1D). Importantly, however, the iTRF mice preserved lean mass (Figure 1D). Blood glucose levels measured at ZT3 (fed) and ZT21 (fasted) trended lower in iTRF versus Ad Lib mice, whereas blood 3OHB levels rose in the iTRF group during each fasting period (ZT21) (Figure 1E). As expected, the iTRF group had improved glucose tolerance at the end of the weekly TRF regimen (Figures S1I–S1K) and dramatically reduced insulin levels (Figures S1L and S1P) during an oral glucose tolerance test (OGTT). Improved insulin sensitivity was evident even after the 3-day recovery period (Figures S1M–S1P) during which iTRF mice consumed more energy per g body mass than their Ad Lib counterparts (Figure 1B). Among the unique elements of the current study, we aimed to test the hypothesis that mice adapted to iTRF would exhibit metabolic resilience during an acute fasting challenge (AFC), performed on all mice at week 8 of iTRF (Figures S1A and 1A–1C). Aligned with the prediction, iTRF mice better retained lean mass at the expense of fat mass during the fasting arm of the AFC (Figure 1F) and fully recovered total body weight during the refeeding arm, whereas the Ad Lib group did not (Figure 1G). Total energy expenditure was unaffected (Figures S1F–S1H). The apparent resilience of the iTRF mice during an AFC was accompanied by remarkable stabilization of blood glucose levels and a robust shift in system flux of the principal ketone, 3OHB (Figure 1H).

Considering that muscle tissues contribute substantially to whole-body lean mass, insulin sensitivity, and systemic glucose tolerance, we proceeded to examine the impact of iTRF on the skeletal muscle proteome. Muscle tissues were harvested after all mice were exposed to a 12-h fast and subsequently assayed by mass spectrometry using TMT-based quantitative proteomics methods. The analysis quantified 2,888 total proteins, of which 319 increased and 150 decreased in response to iTRF at a 5% FDR (Figure 1I). Prominent among the biological processes that emerged from a pathway analysis of significantly changing proteins were several related to mitochondrial energy metabolism, protein translation, and autophagy (Figure 1J). Most notably, a large cluster of proteins related to mitochondrial ribosomes and mRNA processing were upregulated in muscles from iTRF mice (Figures 1K–1L). By contrast, many proteins involved in oxidative phosphorylation (OXPHOS) and the tricarboxylic acid cycle (TCAC) were downregulated (Figure 1L), while enzymes involved in short-chain carbon metabolism, including ketolysis and amino acid catabolism, were either increased or unchanged (Data S1). Surprisingly, the pathway of long-chain FAO was not upregulated, and instead, subtle changes in several enzymes involved in regulating mitochondrial fatty acid transport suggested this process was dampened by iTRF (Data S2). Likewise, targeted metabolite profiling showed muscles and plasma from iTRF mice had modestly diminished levels of even chain acylcarnitines (biomarkers of incomplete beta-oxidation) (Figure 1M). Nonetheless, exercise tolerance was preserved (Figures S1Q and S1R). In sum, the overall proteomic and metabolic signatures suggested that muscles from mice exposed to iTRF adapted in a manner that re-routes carbons toward biosynthetic pathways while dampening oxidative metabolism and/or possibly promoting metabolic efficiency.

(C) Body mass (BM) pre-special diet (e.g., standard chow diet, pre-diet), post-special diet (post-diet), and at TRF weeks 1–9 at ZT3 or ZT21.
(D) BM gained represented as a sum of fat mass (FM) and lean mass (LM).
(E) Blood glucose (BG, top) and blood 3OHB (bottom) post-special diet and at TRF weeks 2–9 at ZT3 or ZT21.
(F) Acute fasting challenge (AFC) change (Δ) in BM, FM, and LM from fed to fasted (fasting) and fasted to refed (refed).
(G) AFC BM change from baseline.
(H) AFC BG, non-essential fatty acids, and 3OHB.
(I) Volcano plot of skeletal muscle (SkM, quadriceps) proteomics.
(J) Proteomics pathway analysis.
(K) Volcano plot of SkM mitochondrial (mito) proteins.
(L) Number of SkM mito proteins up- or downregulated by pathway.
(M) Heatmap of 12-h fasted quadriceps muscle (SkM) metabolites represented as the mean *Z* score.
ZT, zeitgeber time. Data are mean ± SEM (B–H). n = 2–6 per group (B). Mice were group housed; thus, data represent an estimate of food intake per day per mouse. n = 10 per group (C–H). Data were analyzed by two-tailed Student's t test. Asterisk (*) indicates significant difference between Ad Lib and TRF mice. n = 4–5 per group. *$p_{adjusted} \leq 0.05$ (I–L). n represents biological replicates.
See also Figure S1.

Ketone flux in skeletal muscle depends on fiber type and fuel supply

Researchers have speculated that ketones might play a key role in mediating the metabolic benefits of feeding regimens that mimic fasting physiology.[4,6,22] Still, the importance of ketone metabolism (Figure 2A) in muscle and heart in the context of TRF and/or IF has heretofore remained largely unexplored. To address this knowledge gap, incubated soleus (SOL; red/oxidative) and extensor digitorum longus (EDL; white/glycolytic) muscles were exposed to buffer conditions designed to mimic either a fasted or fed state nutrient milieu (Figure 2B) and stable isotope-based metabolic flux analysis (MFA) was performed using [U-^{13}C]3OHB as the tracer (Figure 2C). Muscles were harvested from either overnight fasted or fed mice to ascertain the potential regulatory impact of an acute fast on 3OHB oxidation (Figure 2B). Results from MFA performed in fasted buffer using muscles from fasted mice revealed a striking fiber-type-dependent difference in ketolytic flux (Figures 2D–2F). First, 3OHB measured within the muscle tissues was diluted more in SOL compared with EDL (Figure 2D). Thus, reverse beta-hydroxybutyrate dehydrogenase 1 (BDH1) flux from unlabeled AcAc to unlabeled 3OHB was clearly evident in the red muscles and minimally detectible in white muscles. Likewise, even in the presence of high fat concentrations, flux of ^{13}C-labeled 3OHB into several TCAC intermediates, including citrate, approached an average enrichment of 15% versus 3% in SOL and EDL, respectively (Figure 2E). The difference between muscle types was further amplified when citrate labeling was corrected for the foregoing label dilution of 3OHB (Figure 2F), which accounts for potential disparities in mitochondrial content and/or ketone transport.[23] Similar MFA performed using fed versus fasted buffer (Figures 2G and 2H) and mice (Figures S2I and 2B) showed that muscle ketone flux is driven primarily by exogenous fuel supply, rather than fasting-induced intrinsic adaptions in muscle metabolism. In these resting/quiescent SOL muscles, the fasting-mimetic buffer favored forward ketone flux into the TCAC whereas the fed-state buffer favored reverse BDH1 flux from AcAc to 3OHB (Figures S2E and S2F). The striking fiber-type differences in 3OHB flux were explained by the finding that protein abundance and enzyme activity of the ketolytic enzyme BDH1 were remarkably enriched in mitochondria isolated from highly oxidative muscles (red gastrocnemius and heart) as compared with a more glycolytic muscle (white gastrocnemius) (Figures 2J and 2K). By contrast, the enzymes that catalyze the second and third steps in ketolysis, SCOT and ACAT1, were similarly abundant regardless of the tissue source of mitochondria (Figure 2J). Interestingly, however, protein levels of the ketothiolase enzyme associated with oxidation of medium- and short-chain fatty acids (Acaa2/MKT) were elevated in mitochondria from heart and red muscle as compared to white muscle, similar (but not identical) to BDH1 (Figure 2J).

Muscle BDH1 deficiency compromises exercise tolerance and exacerbates metabolic bottlenecking during acute fasting

The foregoing findings raised the following provocative questions: (1) Why is BDH1 more important to "red" mitochondria, which have robust fat oxidation machinery? (2) Is muscle BDH1 (mBDH1) essential during acute fasting? (3) Does BDH1 flux play a key role in conferring the metabolic benefits of iTRF? To address these fundamental questions, mice in which the *Bdh1* gene was ablated specifically in skeletal and cardiac muscles (mKO) (Figures S3A, S3B, and 3A) were subjected to an AFC and an ensuing graded treadmill test. As compared with their floxed control (FC) littermates, mKO mice had ~30% elevated fasting blood levels of 3OHB (Figure 3C) and reduced exercise tolerance (Figure 3D). Thus, muscle appears to be a major site of 3OHB clearance and ketone fuels play a crucial role in optimizing contractile performance during energy stress. Diminished exercise tolerance was not accompanied by more severe fasting and/or exercise-induced hypoglycemia (Figure 3E). Likewise, we found no genotype-dependent differences in fasting-induced phosphorylation of the pyruvate dehydrogenase (PDH) complex (Figure S3B). Instead, targeted metabolic profiling of heart and skeletal muscles harvested from overnight fasted mice indicated that BDH1 deficiency resulted in elevated fatty acid-derived acylcarnitine intermediates in all three tissues, whereas the opposite pattern was evident in the plasma (Figure 3F). Considering that these metabolites report on bottlenecks in the beta-oxidation pathway and are well recognized as biomarkers of mitochondrial stress, the findings imply that BDH1 has a role in modulating FAO flux in striated muscles and systemically.

The interplay between 3OHB and muscle FAO flux was further examined using the small muscle incubation system coupled with a parallel tracer design to examine the impact of mKO on metabolism of [U-^{13}C]-labeled 3OHB, AcAc, and palmitate (PA) (Figures 3G and 3H). 3OHB contribution to the acetyl pool, measured via acetylcarnitine (C2AC; derived from acetyl-CoA) and citrate (a marker of TCAC flux), was almost fully abrogated in mKO muscles (Figure 3I). However, total ketone flux into each of these pools was largely maintained due to a compensatory increase in flux of exogenous AcAc through the SCOT reaction. Thus, in mKO SOL muscles total ketone contribution to C2AC was unchanged, whereas labeling of citrate decreased 27% compared to the FC group. This decline in ketone-supported TCAC flux in mKO SOL muscles was accompanied by a modest rise in palmitate labeling of both C2AC and citrate (Figure 3J), consistent with a shift toward increased fatty acid catabolism.

Additional insights into the interplay between ketolysis and FAO were gained via analysis of labeled beta-hydroxybutyrylcarnitine (C4OH-AC), a short-chain metabolite that can be derived from all three of the foregoing substrates (Figure 3H). In mKO muscles, 3OHB contribution to C4OH was essentially undetectable and fully replaced by labeling from exogenous AcAc, while palmitate labeling of C4OH was unchanged (Figure 3K). Interestingly, analysis of the mass isotopomer distribution (MID) showed mBDH1 deficiency resulted in lower levels of ketone-derived C4OH labeled with only two heavy carbons (M2) (Figure 3L). The path to M2 C4OH from U^{13}C[ketones] requires ketolysis to acetyl-CoA and subsequent reverse flux of M2 acetyl-CoA to M2 C4OH (Figure 3H). Thus, the pattern observed in mKO SOL is indicative of diminished reverse flux of ketone-derived acetyl-CoA to C4OH. This observation is notable because a recent study discovered that these metabolites participate in a bidirectional short-chain carbon circuit that enhances FAO

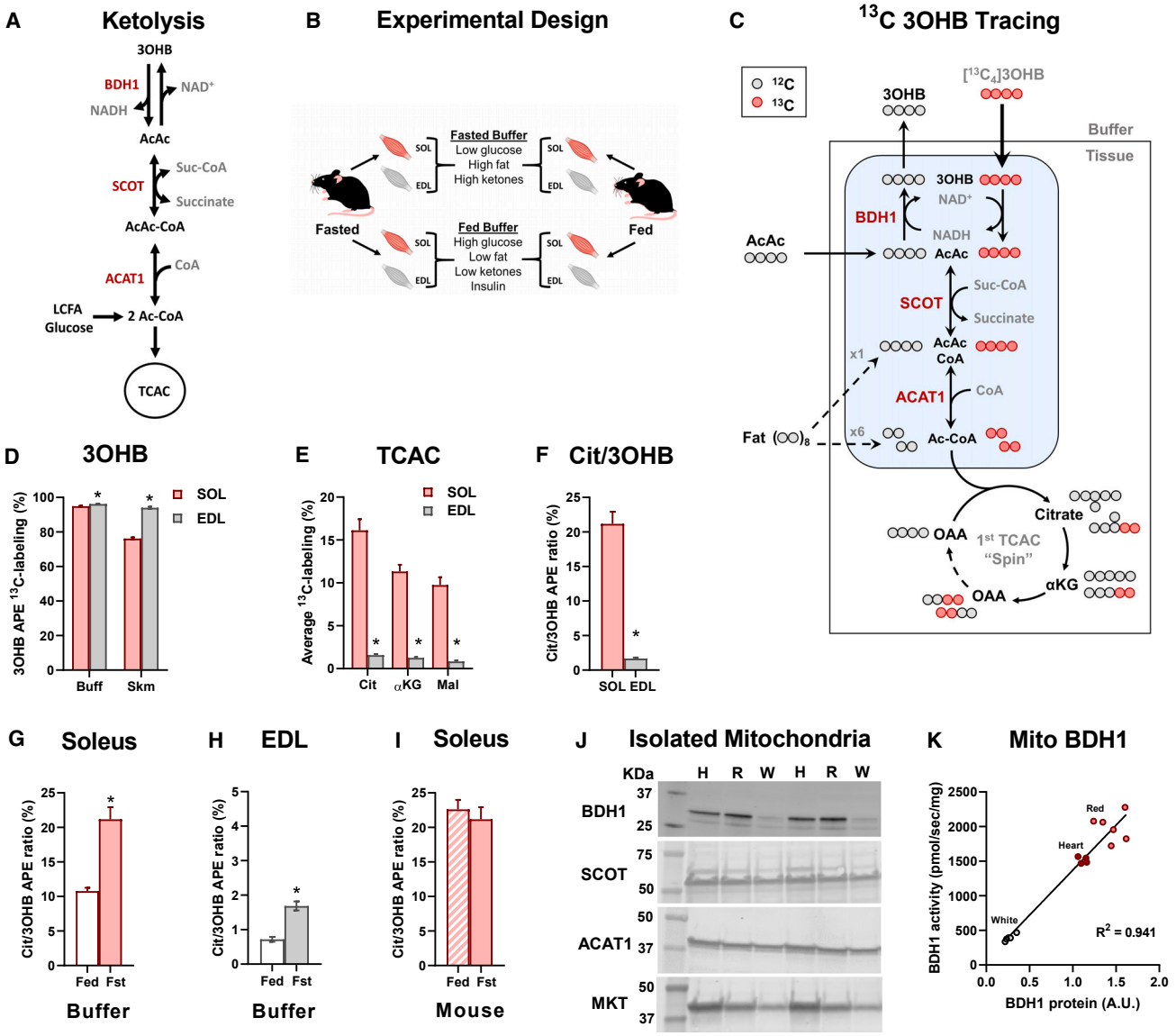

Figure 2. Ketone flux in skeletal muscle depends on fiber type and fuel supply

(A) Ketone oxidation pathways in muscles.

(B) [U-^{13}C] 3OHB tracing experimental design.

(C) SOL and EDL [U-^{13}C] 3OHB labeling strategy. M4 3OHB generates M2 acetyl-CoA and M2 citrate. M2 Ac-CoA derived from 3OHB can be converted to M2 3OHB.

(D) Buffer and tissue 3OHB average ^{13}C labeling (%) from fasted SOL and EDL muscles incubated in fasted buffer.

(E) Average ^{13}C labeling (%) of TCAC intermediates from fasted SOL and EDL muscles incubated in fasted buffer.

(F–I) Citrate (Cit) enrichment normalized to tissue 3OHB labeling from (F) fasted SOL and EDL muscles incubated in fasted buffer, (G) SOL and (H) EDL muscles incubated in fed or fasted (fst) buffers, and (I) SOL muscles isolated from fed or fasted mice incubated in fasted buffer.

(J) Ketolytic enzyme abundance in mitochondria isolated from heart (H), red muscle (R), and white muscle (W).

(K) Correlation plot of BDH1 enzyme activity versus BDH1 protein abundance.

Data are means ± SEM, n = 5–6 per group. Data were analyzed by two-tailed Student's t test. Asterisk (*) indicates significant differences between soleus versus EDL or fed versus fasted buffers (D–I). Representative image with n = 2/tissue type (J). n = 5 per group. Data were analyzed by linear regression. *p ≤ 0.05 (K). n represents biological replicates.

See also Figure S2.

respiratory efficiency in heart and red skeletal muscles by buffering the mitochondrial pools of free CoA and NAD$^+$ (Figure 3M).[24] Reverse flux through MKT and short-chain hydroxyacyl-CoA dehydrogenase (SCHAD) regenerates both free CoA and oxidized NAD$^+$, respectively, which in turn opposes CoA trapping in FAO intermediates and thereby mitigates risk of severe bottlenecks in the beta-oxidation spiral.[24] In the previous report, pyruvate was shown to be a major contributor to reverse

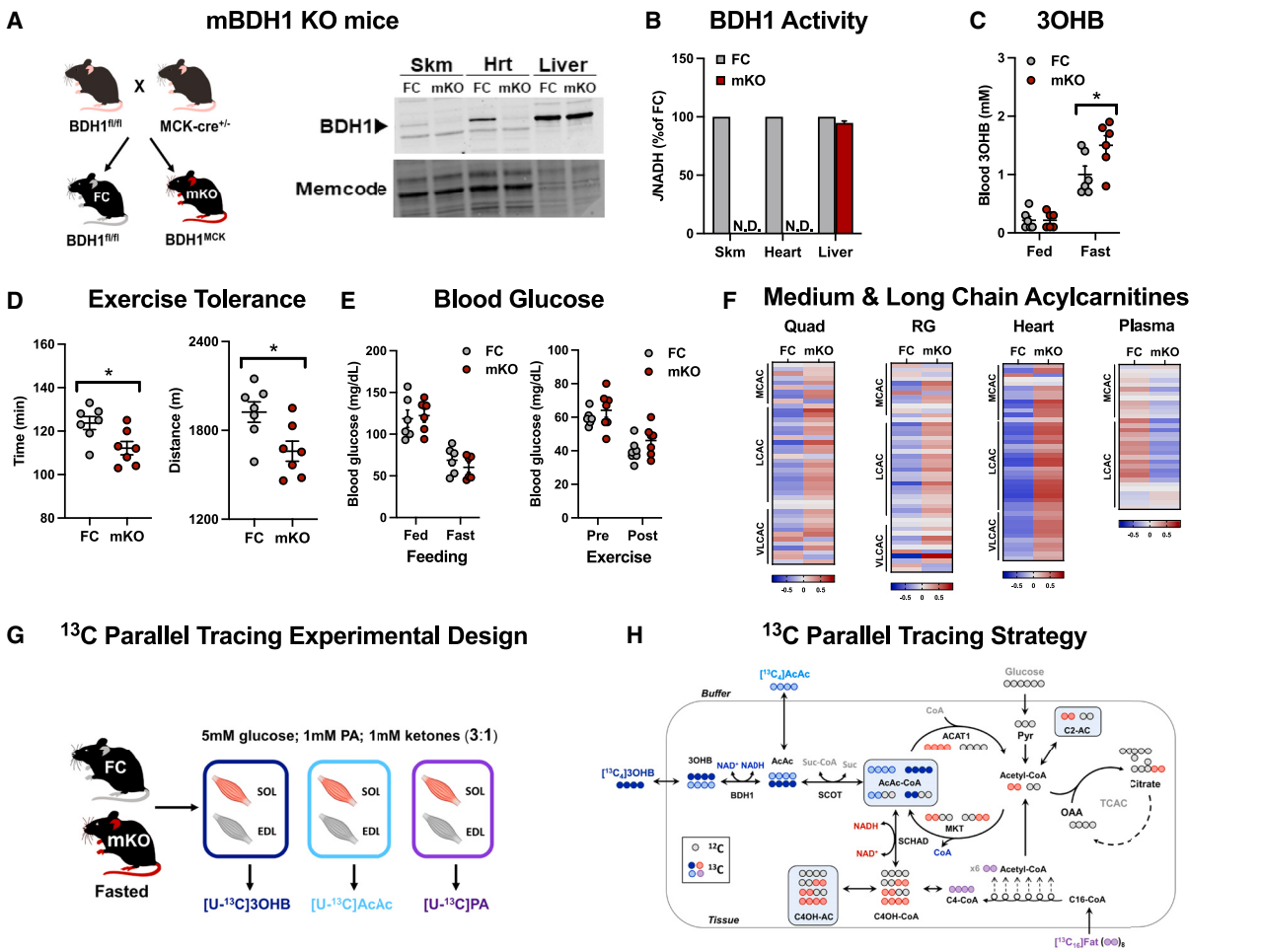

Figure 3. mBDH1 deficiency compromises exercise tolerance and exacerbates metabolic bottlenecking during acute fasting

(A) Mouse model of skeletal muscle (SkM) and heart (Hrt) BDH1 deficiency (mBDH1 KO mice, left) and western blot validation (right).

(B) BDH1 activity in mitochondria from mixed SkM (gastroc and quad), heart, and liver from 18-h fasted mice.

(legend continued on next page)

MKT flux and the accompanying FAO efficiency when glucose availability is plentiful.[24] Here, we discovered that ketones contribute substantially to this circuit during exposure to fasting conditions (Figure 3L). Importantly, this circuit is much less active in white muscles (e.g., EDL; Figures S3C–S3E) due to diminished MKT expression[24] (Figure 2J) and appears to be compromised in red muscles (e.g., SOL) lacking BDH1 (Figure 3L). Disruption of the short-chain carbon circuit in mKO SOL muscles was accompanied by an expansion of the total AcAc and C4OH pools but a diminution in the total C2 pool (Figure 3N). This metabolite pattern is consistent with a bottleneck in FAO and aligns with the cardiac and skeletal muscle acylcarnitine profiles (Figure 3F). In sum, although increased use of exogenous AcAc to support forward SCOT flux in mKO muscles appears to compensate substantially for the block in 3OHB oxidation, loss of BDH1-mediated carbon and redox buffering capacity resulted in more severe fasting-induced accumulation of medium- and long-chain acylcarnitine intermediates and diminution of the muscle acetyl pool.

Cardiac BDH1 deficiency leads to metabolic bottlenecking upon fasting and lipid exposure

Based on the BDH1 protein abundance pattern shown in Figure 2J and the acylcarnitine profiles presented in Figure 3F, we surmised that the FAO bottleneck caused by BDH1 ablation would be most severe when energy demand and fatty acid flux are elevated due to myocyte contraction. To test this prediction, we proceeded to perform MFA on isolated, spontaneously beating hearts perfused in the Langendorff mode with "fasted state" buffer containing [U-^{13}C]-labeled PA (Figures 4A and 4B). The resulting metabolite profiles strongly agreed with the predicted outcomes. Thus, similar to the results of experiments performed in isolated SOL muscles (Figure 3), loss of BDH1 activity in cardiomyocytes was accompanied by increased palmitate labeling of TCAC intermediates (Figures 4C and 4D) and even chain acylcarnitines, including C2AC (Figure 4E), along with marked expansion of the total long- and medium-chain acylcarnitine pools (Figure 4E). Notably, despite this increase in FAO flux, the total pool of C2AC decreased, consistent with FAO bottlenecking. Here, the experiments performed with perfused hearts provided sufficient tissue for measurements of ^{13}C-labeled and total acyl-CoAs (Figures 4F and 4G), which aligned well with the labeling of the corresponding short-chain acylcarnitines. Moreover, the results confirmed the anticipated diminution of the acetyl-CoA pool size and revealed a trend toward a reduction in the free CoA pool (Figure 4H). Overall, the stable isotope tracer analyses showed that despite robust FAO capacity in mitochondria resident in red muscle and heart,[24] increased FAO flux could not fully compensate for the lack of BDH1 flux, which likely contributed to reduced exercise tolerance.

Muscle BDH1 flux is required for iTRF-induced building of lean mass

Next, we proceeded to investigate the contribution of mBDH1 flux to chronic adaptations to iTRF using a 2 × 2 study design (Figure 5A). Interestingly, mBDH1 was not required for the iTRF-induced adaptations that confer profound shifts in whole-body energy balance and insulin sensitivity during a GTT (Figures S4A–S4F), or the blunted oscillations in blood glucose and circulating 3OHB during an AFC (Figures 5B and 5C). Although mKO mice tended to gain slightly less weight than the FC group throughout the duration of the study (Figure 5D), differences between genotypes did not reach statistical significance. Body composition analyses showed that iTRF resulted in a similar pattern of diminished fat mass accrual, regardless of genotype (Figure 5E). Remarkably, however, whereas the iTRF regimen led to progressively increased lean body mass in the FC mice, this effect was absent in the mKO group (Figure 5F). The genotype-specific changes in lean mass resembled those observed in the weights of excised EDL muscles (Figure 5G).

Based on evidence linking mBDH1 to adaptations in lean mass (Figure 5F) as well as net reverse flux of AcAc in muscles exposed to a fed-state nutrient milieu (Figure S2F), we sought to test the hypothesis that 3OHB flux might alter carbon trafficking through other redox-sensitive enzymes (e.g., PDH, MDH, and GDH) during transitions between fasting and refeeding. To this end, MFA was performed using [U-^{13}C]glucose in the context of the fed-state-mimetic buffer provided to small muscles excised from FC and mKO mice subjected to iTRF or fed Ad Lib (Figures 5H and 5I). The average ^{13}C enrichments measured in tissue pyruvate and TCAC metabolites were similar among the four treatment groups. Notably, iTRF increased glutamine (Gln) labeling in FC, but not mKO, mice (Figures 5J–5L). By contrast, relative glucose flux into C2 and C4OH acylcarnitines, both derived from an acetyl-CoA pool linked to PDH, was diminished in mKO SOL muscles regardless of the feeding regimen (Figures 5M and 5N). Additionally, close evaluation of the MIDs

(C) Blood 3OHB in fed and 18-h fasted states.
(D) Time and distance to exhaustion during a treadmill test after an 18-h fast.
(E) Blood glucose before and after the exercise test.
(F) Acylcarnitine profiles of quadriceps (Quad), red gastrocnemius (RG), heart, and plasma from mice in the 12-h fasted state represented as mean of the *Z* score.
(G and H) ^{13}C parallel tracing experimental design (G) and ^{13}C parallel tracing strategy (H) in fasted SOL and EDL muscles from mice incubated in fasted buffer with ^{13}C 3OHB (dark blue), ^{13}C AcAc (light blue), or ^{13}C palmitate (PA, purple).
(I and J) Ketone (I) and palmitate (J) ^{13}C labeling (%) in fasted SOL.
(K) C4OHAC average ^{13}C labeling (%) in fasted SOL.
(L) C4OHAC labeling from ketones (^{13}C 3OHB+ ^{13}C AcAc) as MIDs.
(M) Short-chain (SC) carbon circuit in SkM.
(N) Semi-quantitative estimate for metabolite pool sizes of AcAc, C4OH AC, and C2AC in fasted SOL. Metabolite peak areas were normalized to internal standard peak areas (norvaline, AcAc; d_9-carnitine, C4OH AC and C2AC) and tissue mass.
Data are means ± SEM (B–E, I–L, and N). Representative image with n = 1 (A) and 4 (B) per group. n = 6–8 per group. Data were analyzed by two-tailed Student's t test. Asterisk (*) indicates significant differences between FC and mKO mice. *p $\leq$ 0.05 (C–F, I–L, and K). n represents biological replicates.
See also Figure S3.

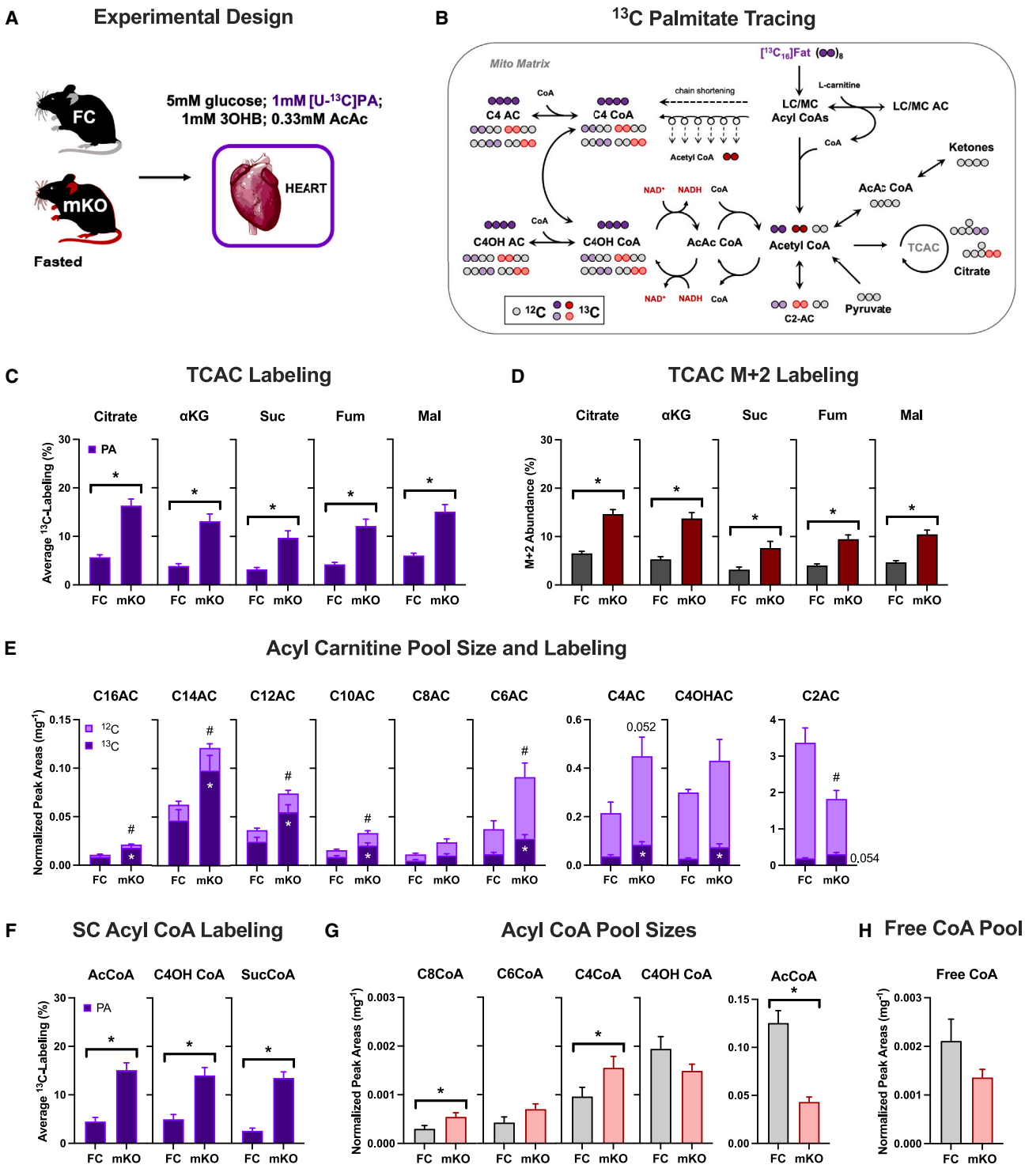

Figure 4. Cardiac BDH1 deficiency leads to metabolic bottlenecking upon fasting and lipid exposure

(A and B) ^{13}C-tracing experimental design (A) and ^{13}C-palmitate (PA) tracing strategy (B) in fasted, Langendorff-perfused hearts.

(C) TCAC intermediate ^{13}C labeling (%) in fasted hearts.

(D) M+2 abundance (%) in TCAC intermediates.

(E) Semi-quantitative estimate for pool sizes of acylcarnitines in fasted hearts. Acylcarnitine peak areas were normalized to d_9-carnitine standard and tissue mass. Acylcarnitine pool sizes are segregated by the tracer-derived contribution (^{13}C, dark purple) and the unlabeled fraction (^{12}C, light purple).

(F) Short-chain acyl-CoA labeling (%) in fasted hearts.

(legend continued on next page)

revealed that SOL muscles from FC, but not mKO, mice increased the citrate fraction with 5 heavy carbons (M5 citrate) upon adaptation to iTRF (Figure 5O). This labeling pattern is suggestive of iTRF-induced increases in pyruvate anaplerotic flux (Figure 5I) and was further supported by the robust increase of Gln with 2–5 heavy carbons (M2-M5 Gln) (Figure 5P). Also noteworthy is that the citrate and Gln labeling patterns measured in FC/iTRF muscles are reminiscent of those observed in other models of growth and hypertrophy.[25] In sum, these results show that net flux through mBDH1 during feeding and/or refeeding impacts mitochondrial trafficking of pyruvate.

Deficiency of BDH1 in heart and red skeletal muscles compromises iTRF-induced mitochondrial remodeling

To complement the ^{13}C MFA conducted with excised small muscles, parallel experiments were performed using isolated mitochondria and a recently developed platform for comprehensive assessment of respiratory power and efficiency. The platform leverages a modified version of a creatine kinase (CK) energetic clamp technique that titrates the extramitochondrial ATP:ADP ratio (i.e., free energy of ATP hydrolysis [ΔG_{ATP}]) and thereby permits precise control of energy demand within a near-physiological range.[26,27] In simple terms, this technique serves as an *in vitro* "stress test" that evaluates mitochondrial respiratory responses to a graded energetic challenge, akin to transitions between rest and exercise *in vivo* (Figure 6A). Analysis of the linear relationships between (1) energy demand (ATP:ADP, ΔG_{ATP}) and steady-state oxygen flux (JO_2), and (2) JO_2 and mitochondrial membrane potential ($\Delta\Psi_m$) allows for respective estimations of respiratory conductance (wherein a steeper slope indicates reduced resistance and improved kinetics) and respiratory efficiency (wherein a rightward shift indicates enhanced efficiency and improved thermodynamics) (Figures 6B and 6C). The bulk of these experiments centered on heart because cardiac tissue provides a plentiful source of BDH1-enriched mitochondria.

Results of the MFAs revealed three major phenotypes that were affected by an interaction between iTRF and genotype. First, despite what appeared to be a dampening of oxidative machinery in response to iTRF (Figures 1I–1L), heart mitochondria from FC mice retained respiratory conductance and maximal oxygen consumption (Figure 6D), regardless of the feeding regimen and respiratory substrates provided (fatty acid, pyruvate, or mixed fuels). By contrast, mitochondria from mKO heart had diminished respiratory conductance (decreased slope) in the presence of all three fuel combinations. Second, in FC mitochondria, iTRF tended to shift the respiratory efficiency plots rightward, whereas in mKO mitochondria the plots shifted leftward, regardless of the substrate setting (Figure 6E). Similar outcomes were observed in mitochondria isolated from red gastrocnemius muscles, whereas the genotype differences were less pronounced in mitochondria from white gastrocnemius (Figure S5). The leftward shift in the efficiency plots indicates that mKO mitochondria were maintaining a lower (less polarized) $\Delta\Psi_m$ for any given rate of oxygen consumption, suggesting these mitochondria are less poised to defend bioenergetic stability *in vivo* when confronted with energy and/or nutrient stress. Third, concurrent measurements of electron leak (JH_2O_2/JO_2) were performed as an index of reactive oxygen species (ROS)-emitting potential. These assays revealed that the iTRF regimen remodeled mKO heart mitochondria in a manner that increased ROS-emitting potential, but this effect was absent in FC mice (Figure 6F).

Synthesis of the experimental outcomes presented in Figures 1, 2, 3, 4, and 5 implied that iTRF leads to remodeling of muscle tissues and their resident mitochondria, which in turn affects carbon partitioning, respiratory efficiency, and lean mass. Moreover, the results predict that optimal mitochondrial remodeling in response to iTRF requires BDH1 flux. Consistent with this premise, mass spectrometry-based proteomics of semi-purified cardiac mitochondria (Figure 7A) identified a subset of mitochondrial proteins for which adaptations to the feeding regimen depended on BDH1 activity (Data S3). Notably, when comparing cardiac mitochondria derived from FC and mKO mice at baseline, BDH1 emerged as the only protein differentially abundant between genotypes (Figure 7B). Next, using label-free proteomics and an FDR cutoff of 5%, comparison of the TRF effects in each genotype revealed more upregulated proteins (iTRF/Ad Lib; Figure 7C) detected in mitochondria isolated from FC hearts (Figure 7C), in contrast to more downregulated proteins in the mKO group (Figure 7D). The analysis identified 113 of 690 total mitochondrial proteins that changed significantly ($q < 0.1$) in at least one of the two genotypes (Data S3). Top ranked among proteins that were uniquely downregulated in mKO included Pcca and Acot9, which have roles in regulating amino acid metabolism; Coq3, Uqcrc2, and Brawnin, each involved in the electron transport system; and Ghitm, Mrpl32, Dars2, and Lonp1, which participate in mitochondrial proteostasis. In aggregate, the findings corroborate the conclusion that loss of mBDH1 flux disrupts iTRF-induced tissue and mitochondrial remodeling in both heart and skeletal muscle.

DISCUSSION

Whereas previous studies have reported that TRF promotes muscle function in *Drosophila* models of obesity,[28,29] to our knowledge the current study provides original evidence that iTRF leads to broad remodeling of the muscle proteome in mice, coincident with increased lean body mass. Also noteworthy is that the salutary effects of iTRF on whole-body and skeletal muscle metabolism did not require a backdrop of high-fat-diet-induced obesity, implying that this regimen could have benefits in humans classified as normal weight. Most notably, this investigation provides first-time evidence that ketones and mBDH1 flux are indeed required for conferring the full adaptive benefits of iTRF, including increased lean mass and mitochondrial hormesis. The results also reveal an intriguing

(G and H) Semi-quantitative estimate for pool sizes of acyl-CoAs (G) and free CoA (H) in fasted hearts. Acyl-CoA and free CoA peak areas were normalized to d_9-pentanoyl-CoA standard and tissue mass.

Data are represented as means ± SEM. n = 7–9 per group and data were analyzed by two-tailed Student's t test. Asterisk (*) indicates significant differences between FC and mKO mice. *$p \leq 0.05$ (C–H). Asterisk (*) and pound sign (#) represent genotype differences ($p \leq 0.05$) between ^{13}C-labeled fraction and unlabeled fraction, respectively (E).

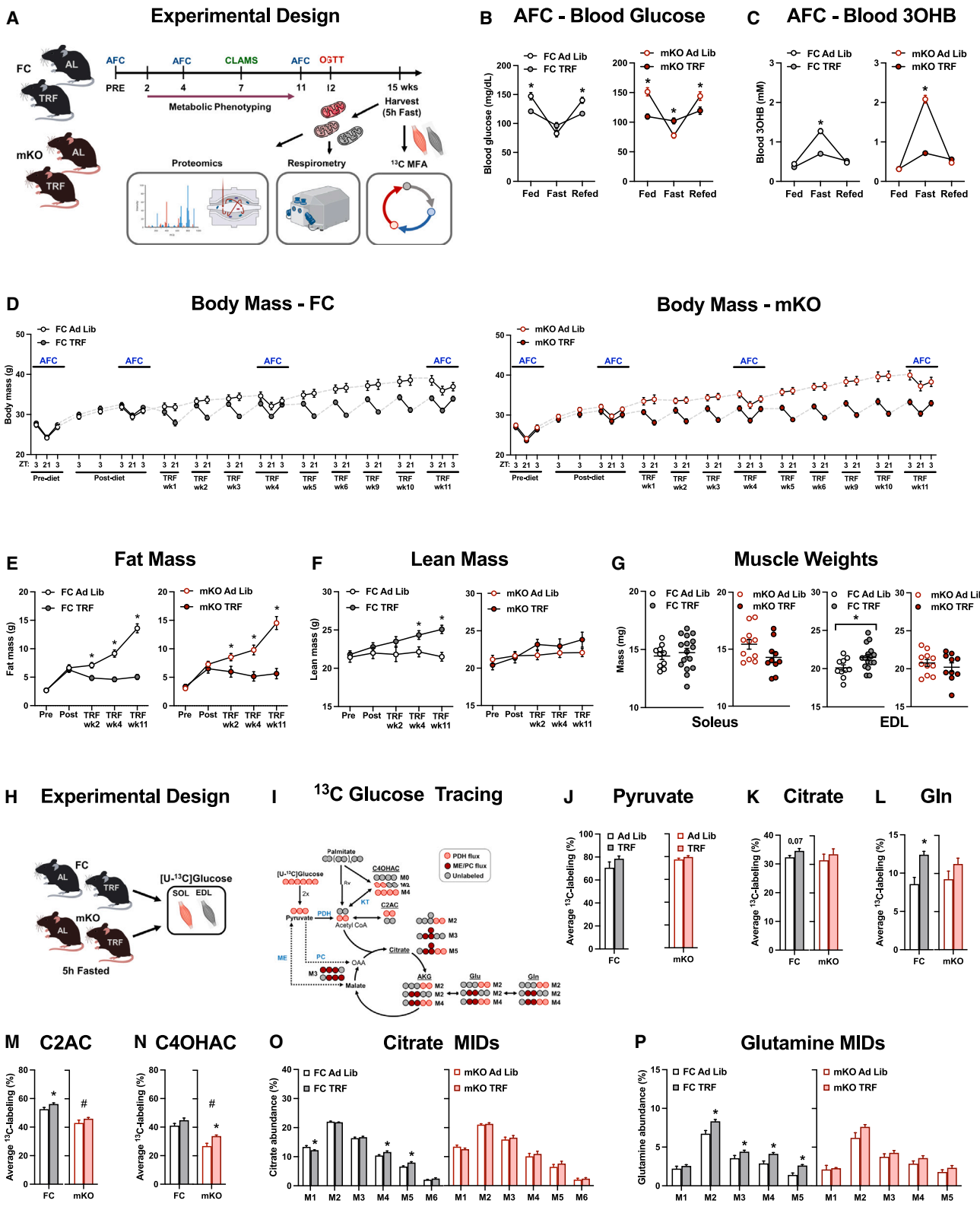

Figure 5. Muscle BDH1 flux is required for iTRF-induced building of lean mass

(A) iTRF experimental design in FC and mKO mice.

(B and C) Blood glucose (B) and 3OHB (C) during an acute fasting challenge (AFC).

(D–F) Longitudinal measures of (D) body mass, (E) fat mass, and (F) lean mass.

(legend continued on next page)

interplay between ketolysis, efficient FAO, and mitochondrial pyruvate trafficking in muscles exposed to recurring episodes of energy stress and recovery. Thus, 3OHB-supported respiratory efficiency and metabolic rewiring might contribute to the evolutionary advantage imparted by increased BDH1 abundance in highly oxidative cells and tissues.

Importantly, studies in mBDH1 KO mice strongly imply that cardiac and skeletal muscles contribute substantially to ketone clearance during fasting. Moreover, mass spectrometry-based MFA led to the discovery that BDH1 (but not other ketolytic enzymes such as SCOT or ACAT1) is uniquely abundant in mitochondria from red skeletal muscles and heart, raising the question of why this enzyme is distinctly important to highly oxidative fibers that have robust FAO machinery. The answer we uncovered—that BDH1 flux mitigates inefficient FAO—emerged when mKO mice were challenged with physiological settings that promote a switch from glucose to FA fuels (i.e., exercise and fasting). Despite robust capacity for lipid catabolism and compensatory increases in AcAc flux, mKO muscles could not fully compensate for the loss of BDH1, evidenced by impaired exercise tolerance and maladaptive responses to iTRF. Functional deficits in mKO mice were not linked to more severe hypoglycemia but instead to perturbations in FAO. Most remarkably, loss of BDH1 in "red" muscles exacerbates fasting-induced accumulation of lipid-derived acylcarnitine intermediates. These metabolites are generated as byproducts of incomplete beta-oxidation and broadly viewed as biomarkers of metabolic bottlenecking and mitochondrial stress.[30–34] This finding supports the conclusion that BDH1-generated redox potential acts as a mild brake on FAO that in turn tempers metabolic bottlenecks in the beta-oxidation pathway (Figure 7E).

We also found that BDH1 buffers and maintains the mitochondrial acetyl-CoA pool, which not only fuels the TCAC but also provides sufficient driving force for reverse MKT flux. This discovery extends those from a recent study showing that reverse MKT flux in heart and red skeletal muscles defends against FAO bottlenecking and severe CoA trapping.[24] Whereas the earlier report showed that pyruvate feeds this short-chain carbon circuit when glucose is plentiful, the current investigation reveals that 3OHB is critical for maintaining reverse MKT flux during fasting conditions, which presumably optimizes FAO efficiency in muscle mitochondria that are programmed to consume lipid fuels. In addition to supporting the short-chain carbon circuit, forward BDH1 flux during acute fasting supplies electron potential energy for proton pumping at complex I of the ETC, a more oxygen-efficient route to ATP synthesis than the FAD-linked electron flux driven by the first step in FAO.[18,35,36] Conversely, net reverse BDH1 flux during refeeding promotes NAD^+ regeneration, which has the potential to modulate carbon flux through redox-sensitive enzymes such as PDH, IDH, MDH, and GDH.

While the current study centered on the role of muscle/heart BDH1 flux in the settings of acute and chronic exposures to an extended fasting period, previous studies examined links between ketone oxidation and obesity-related glucose intolerance. For example, SCOT was found to be increased in muscles of obese mice, and inhibition of the enzyme via treatment with pimozide or muscle-specific genetic ablation of Oxct1/SCOT reversed obesity-induced hyperglycemia in association with increased PDH activity.[37] These findings raise the possibility that deletion of SCOT, alone or combination with BDH1, might alter TRF-induced effects on glucose homeostasis. Also noteworthy is that targeted disruption of BDH1 in hepatocytes, the main site of ketogenesis (i.e., flux of acetyl-CoA to BOHB), results in a liver phenotype characterized by acetyl0CoA accumulation, reduced succinyl-CoA, and diminished TCAC flux.[38] Thus, it appears that BDH1 also plays a key role in buffering the liver acetyl-CoA/free CoA pools, which in turn affects overall oxidative fluxes.

In aggregate, our results show that BDH1-supported buffering of the short-chain carbon and redox pools in skeletal muscle and heart serves to fine-tune mitochondrial fuel switching during transitions between fasting and refeeding. These mechanisms appear to promote energy stability during acute fasting while also supporting the bioenergetic demands of tissue and organelle remodeling in response to cyclic periods of famine and feasting. Together, the findings establish indispensable roles for ketones and mBDH1 flux in driving favorable adaptations to a dietary regimen that has captured widespread attention for its potential health benefits.

Limitations of the study

Studies involving periodic exposures to fasting physiology fall into a nuanced area of metabolic research, both in terms of the precise feeding schedules and the nomenclature used to describe them (reviewed in Mihaylova et al.[4]). As compared to several other TRF and IF regimens that have been employed by researchers, we developed and tested a new iTRF regimen based on the goals of the study (described in results). To assist readers in understanding how our regimen compares to others, we provide a table (Data S5) summarizing key features and outcomes of various studies on this topic. Our regimen is unique in that we incorporated a 4-day TRF cycle followed by a 72-h recovery period every week. Also noteworthy is that by design, we did not control caloric intake

(G) SOL and EDL muscle weights.
(H and I) Experimental design (H) and tracing scheme (I) for ^{13}C glucose studies in SOL and EDL muscles from 5-h fasted Ad Lib and TRF FC and mKO mice under fed buffer conditions. Light and dark red circles represent carbons from PDH flux or anaplerotic fluxes (malic enzyme [ME] and pyruvate carboxylase [PC]), respectively.
(J–N) Average ^{13}C labeling (%) of (J) pyruvate, (K) citrate, (L) glutamine (gln), (M) C2AC, and (N) C4OHAC.
(O) Citrate (O) and glutamine (P) mass isotopomer distributions (MIDs).
Data are represented as mean ± SEM (B–G and J–P). n = 12–16 (B–D), 10–16 (E and F), 9–16 (G), and 5–8 (J–P) per group. Data were analyzed by two-tailed Student's t test (B–G) or two-way ANOVA (M and N). Asterisk (*) indicates significant differences between FC Ad Lib and FC TRF or mKO Ad Lib and mKO TRF mice. Pound sign (#) indicates main effect of genotype. *$p \leq 0.05$ (J–P). n represents biological replicates.
See also Figure S4.

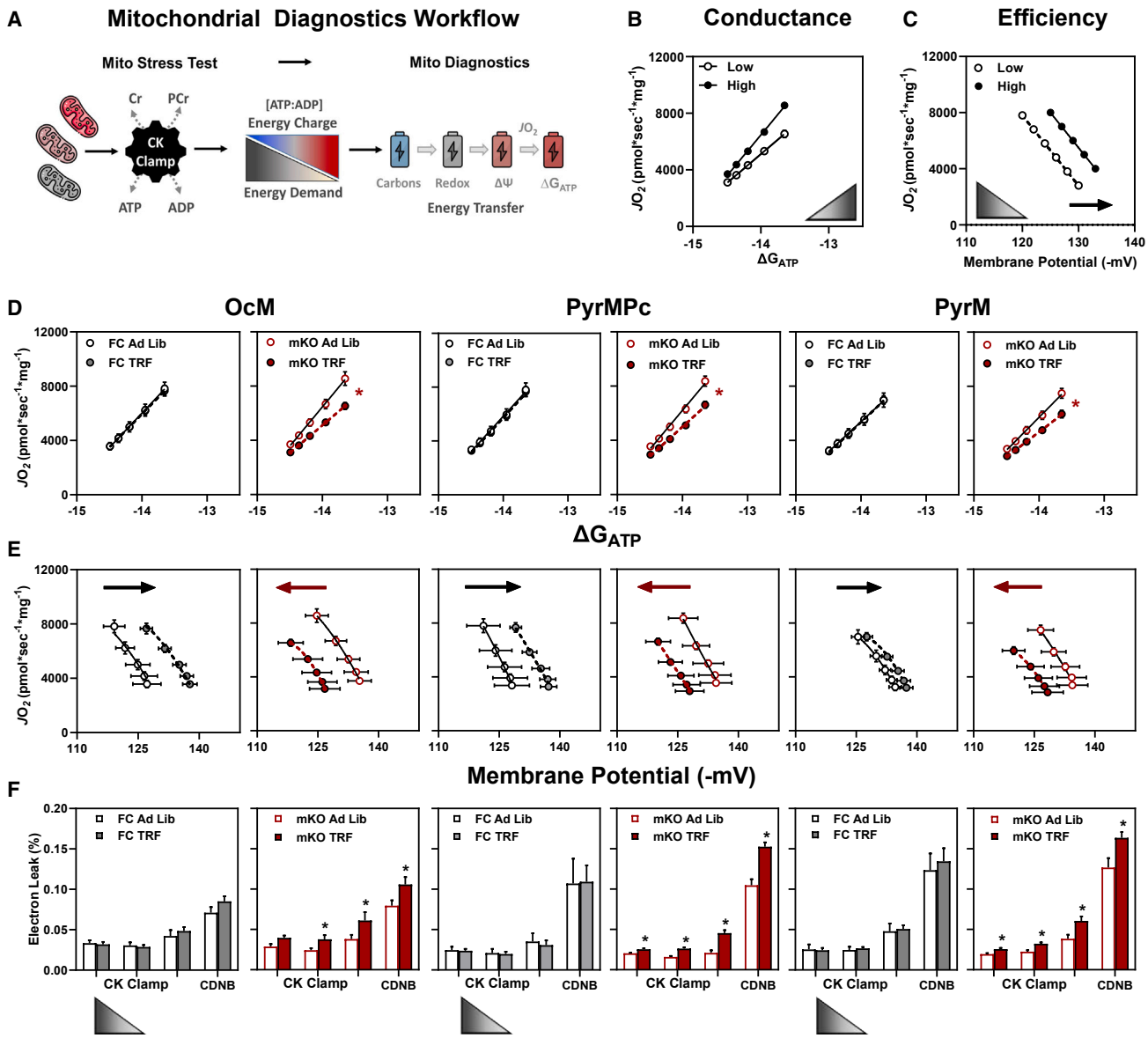

Figure 6. Deficiency of BDH1 in heart compromises iTRF-induced reprogramming of mitochondrial efficiency

(A) Function of freshly isolated heart mitochondria was examined using the Oroboros-O2K respirometry system paired with the creatine kinase (CK) energetic clamp technique. Parallel measurements of membrane potential ($\Delta\Psi$), redox potential (NAD(P)H/NAD(P)+), and JH_2O_2 emissions were obtained via spectrofluorometric assays using a QuantaMaster spectrofluorometer.

(B) Example of respiratory conductance (JO_2 versus Gibb's free energy of ATP hydrolysis or ΔG_{ATP}). A steeper slope represents higher conductance (closed circles) whereas a lower slope indicates lower conductance (open circles).

(C) Example of respiratory efficiency (JO_2 versus $\Delta\Psi$). The rightward shift shows that mitochondria are maintaining a more polarized $\Delta\Psi$ for any given rate of oxygen consumption (JO_2), indicative of increased respiratory efficiency or a higher P:O ratio.

(D–F) JO_2 versus ΔG_{ATP} (D), mitochondrial respiratory efficiency represented as JO_2 plotted against $\Delta\Psi$ (E), and electron leak expressed as a percentage of oxygen flux (F) (JH_2O_2/JO_2*100 = % electron leak) measured in heart mitochondria fueled by octanoyl-carnitine + malate (OcM), pyruvate + palmitoyl-carnitine + malate (PyrMPc), or pyruvate + malate (PyrM).

Data are means ± SEM, n = 5–7 per group (D–F). Data were analyzed by two-tailed Student's t test (F). The black (FC) and red (mKO) arrows indicate the direction of the respiratory efficiency shift. Asterisk (*) indicates significant differences between FC Ad Lib and FC TRF or mKO Ad Lib and mKO TRF mice. *p ≤ 0.05 (E). n represents biological replicates.

See also Figure S5.

and did not examine potential effects of the feeding schedule on circadian rhythms and circadian physiology. Interestingly, despite Ad Lib access to food 3 days/week, the iTRF regimen described herein resulted in reduced caloric intake. Nonetheless, based on commonly used definitions in the literature, our regimen aligns more closely with TRF than caloric restriction

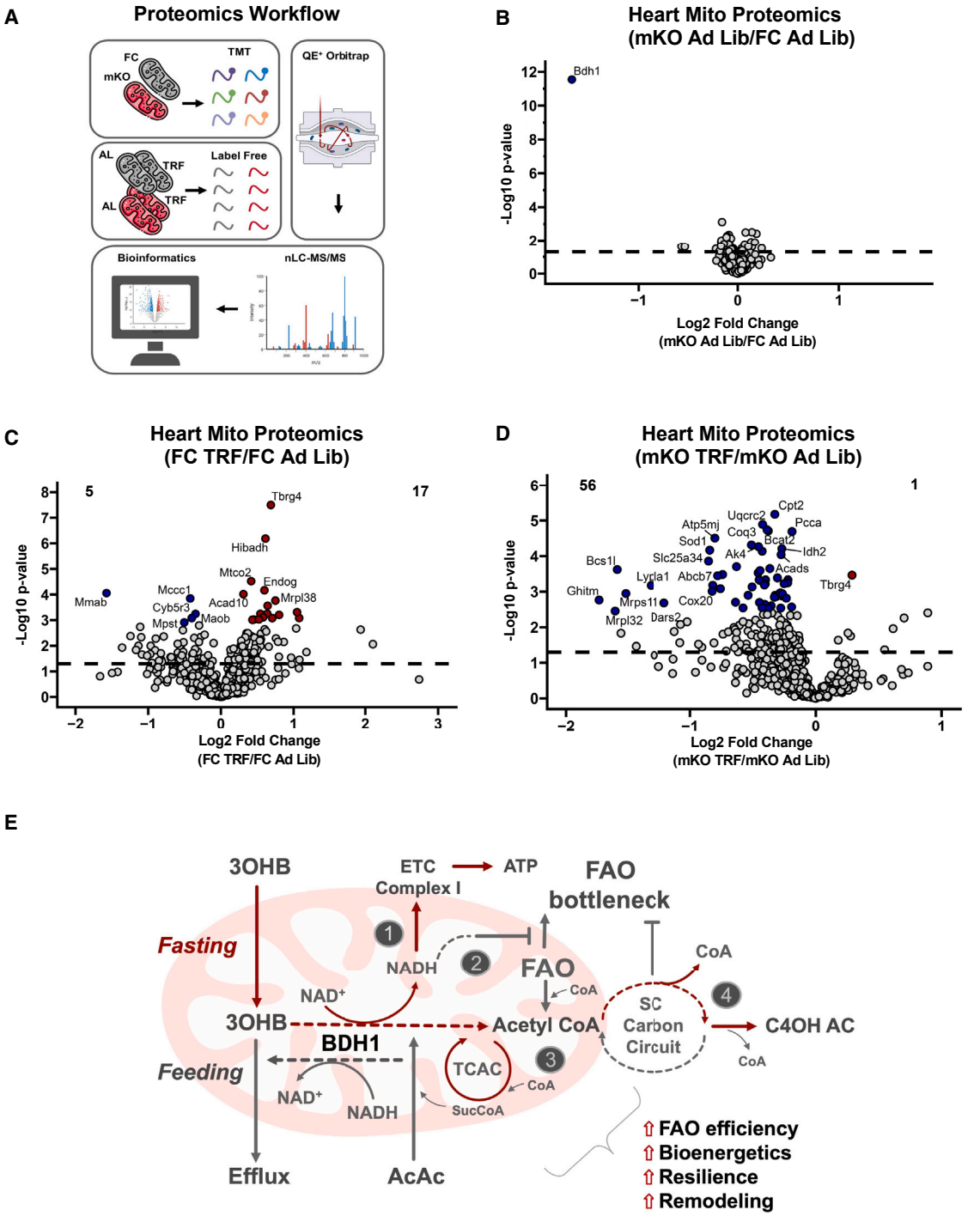

Figure 7. mBDH1 deficiency compromises iTRF-induced remodeling of the cardiac mitochondrial proteome

(A) Proteomics workflow using both TMT and label-free methods.

(B–D) Volcano plot of the mitochondrial proteome derived from hearts of 5-h fasted (B) Ad Lib FC versus Ad Lib mKO mice, (C) Ad Lib versus TRF FC mice, and (D) Ad Lib versus TRF mKO mice. Red and blue circles represent proteins upregulated and downregulated, respectively ($p_{adjusted} < 0.05$). Data are means of the *Z* score. n = 5/group. n represents biological replicates.

(E) Mechanisms by which BDH1 impacts FAO and overall mitochondrial efficiency: (1) redox transfer to complex I optimizes electron partitioning, (2) a mild redox-induced brake fine-tunes beta-oxidation and prevents severe FAO bottlenecking, and (3) provision of acetyl-CoA supports TCAC flux as well as (4) reverse MKT flux, which defends against CoA trapping and bioenergetic instability.

(CR) because we ''limited consumption of food to a short daily window of time,''[4] without an intentional reduction in caloric intake. By contrast, CR refers to a deliberate restriction in calories consumed.[4] Notably, the inadvertent reduction in average weekly caloric intake that was observed in response to iTRF resembles the incidental lowering of energy consumption reported in many human time-restricted eating trials.[4] Moreover, our iTRF regimen allowed access to food during the last 3 h of the dark (active) and first 3 h of the light (inactive) cycle, akin to humans who tend to skip breakfast and consume most calories during evening and late-night hours.[4] Whether or not the same results would emerge given a different schedule and/or an isocaloric approach remains uncertain. Last, because we sought to study ketone metabolism in striated muscles with high levels of BDH1 expression (heart and red skeletal muscles), we used a KO mouse model that targets both tissues. Therefore, we are unable to form firm conclusions about the physiological consequences of ablating BDH1 specifically in either heart or skeletal muscle.

STAR★METHODS

Detailed methods are provided in the online version of this paper and include the following:

- KEY RESOURCES TABLE
- RESOURCE AVAILABILITY
  - Lead contact
  - Materials availability
  - Data and code availability
- EXPERIMENTAL MODEL AND SUBJECT DETAILS
  - Animal studies
- METHOD DETAILS
  - Chemicals and reagents
  - Blood and plasma metabolites
  - Body composition and energy balance
  - Glucose homeostasis
  - Exercise tolerance
  - iTRF mouse harvests
  - Langendorff heart perfusions
  - Isolated skeletal muscle incubations
  - Quantification of 3OHB and AcAc consumption rates
  - Tissue homogenization and extraction
  - GC-MS assay
  - LC-MS/MS for acylcarnitine assay
  - LC-MS/MS for acyl-CoA assay
  - Mitochondrial diagnostics
  - BDH1 activity assay
  - Targeted mass spectrometry-based metabolomics
  - Western blot analysis
  - Proteomic sample preparation
  - Proteomic data acquisition
  - Proteomics data analysis
- QUANTIFICATION AND STATISTICAL ANALYSIS

SUPPLEMENTAL INFORMATION

Supplemental information can be found online at https://doi.org/10.1016/j.cmet.2024.01.007.

ACKNOWLEDGMENTS

We thank the DMPI Metabolomics and Biomarker Core Laboratory for assistance with tissue and plasma metabolomics. The graphical abstract was created with BioRender.com. This work was supported by National Institutes of Health grants 3R01DK089312(D.M.M.), 2R01HL128349 (D.M.M. and D.P.K.), and K01DK125609 (A.S.W.). The DMPI Metabolomics Core Laboratory is supported by Diabetes and Endocrine Research Center grant P30 DK124723.

AUTHOR CONTRIBUTIONS

Conceptualization, D.M.M., A.S.W., and S.B.C.; study design, D.M.M., A.S.W., S.B.C., T.R.K., and G.-F.Z.; methodology, A.S.W., S.B.C., T.R.K., G.-F.Z., S.P.L., P.A.G., and D.P.K.; investigation, A.S.W., S.B.C., T.R.K., G.-F.Z., S.P.L., P.A.G., J.M.J., R.J.W., and D.H.S.; data analysis, statistics, and visualization, D.M.M., A.S.W., S.B.C., T.R.K., S.P.L., P.A.G., J.M.J., and R.J.W.; writing – original draft, D.M.M.; writing – review & editing, D.M.M., A.S.W., S.B.C., T.R.K., G.-F.Z., J.M.J., D.H.S., R.J.W., S.P.L., P.A.G., and D.P.K.; funding acquisition, D.M.M., D.P.K., and A.S.W.

DECLARATION OF INTERESTS

D.M.M. is a member of the *Cell Metabolism* advisory board.

Received: June 15, 2023
Revised: September 20, 2023
Accepted: January 10, 2024
Published: February 6, 2024

REFERENCES

1. Longo, V.D., and Panda, S. (2016). Fasting, circadian rhythms, and time-restricted feeding in healthy lifespan. Cell Metab. *23*, 1048–1059.
2. Lee, M.B., Hill, C.M., Bitto, A., and Kaeberlein, M. (2021). Antiaging diets: separating fact from fiction. Science *374*, eabe7365.
3. Hofer, S.J., Carmona-Gutierrez, D., Mueller, M.I., and Madeo, F. (2022). The ups and downs of caloric restriction and fasting: from molecular effects to clinical application. EMBO Mol. Med. *14*, e14418.
4. Mihaylova, M.M., Chaix, A., Delibegovic, M., Ramsey, J.J., Bass, J., Melkani, G., Singh, R., Chen, Z., Ja, W.W., Shirasu-Hiza, M., et al. (2023). When a calorie is not just a calorie: diet quality and timing as mediators of metabolism and healthy aging. Cell Metab. *35*, 1114–1131.
5. Krízová, E., and Simek, V. (1996). Effect of intermittent feeding with high-fat diet on changes of glycogen, protein and fat content in liver and skeletal muscle in the laboratory mouse. Physiol. Res. *45*, 379–383.
6. Anson, R.M., Guo, Z., de Cabo, R., Iyun, T., Rios, M., Hagepanos, A., Ingram, D.K., Lane, M.A., and Mattson, M.P. (2003). Intermittent fasting dissociates beneficial effects of dietary restriction on glucose metabolism and neuronal resistance to injury from calorie intake. Proc. Natl. Acad. Sci. USA *100*, 6216–6220.
7. Hatori, M., Vollmers, C., Zarrinpar, A., DiTacchio, L., Bushong, E.A., Gill, S., Leblanc, M., Chaix, A., Joens, M., Fitzpatrick, J.A.J., et al. (2012). Time-restricted feeding without reducing caloric intake prevents metabolic diseases in mice fed a high-fat diet. Cell Metab. *15*, 848–860.
8. Chaix, A., Zarrinpar, A., Miu, P., and Panda, S. (2014). Time-restricted feeding is a preventative and therapeutic intervention against diverse nutritional challenges. Cell Metab. *20*, 991–1005.
9. Ulgherait, M., Midoun, A.M., Park, S.J., Gatto, J.A., Tener, S.J., Siewert, J., Klickstein, N., Canman, J.C., Ja, W.W., and Shirasu-Hiza, M. (2021). Circadian autophagy drives iTRF-mediated longevity. Nature *598*, 353–358.
10. Sutton, E.F., Beyl, R., Early, K.S., Cefalu, W.T., Ravussin, E., and Peterson, C.M. (2018). Early time-restricted feeding improves insulin sensitivity, blood pressure, and oxidative stress even without weight loss in men with prediabetes. Cell Metab. *27*, 1212–1221.e3.

11. Gabel, K., Hoddy, K.K., Haggerty, N., Song, J., Kroeger, C.M., Trepanowski, J.F., Panda, S., and Varady, K.A. (2018). Effects of 8-hour time restricted feeding on body weight and metabolic disease risk factors in obese adults: a pilot study. Nutr. Healthy Aging *4*, 345–353.

12. Gill, S., and Panda, S. (2015). A smartphone app reveals erratic diurnal eating patterns in humans that can be modulated for health benefits. Cell Metab. *22*, 789–798.

13. Hutchison, A.T., Regmi, P., Manoogian, E.N.C., Fleischer, J.G., Wittert, G.A., Panda, S., and Heilbronn, L.K. (2019). Time-restricted feeding improves glucose tolerance in men at risk for type 2 diabetes: a randomized crossover trial. Obesity *27*, 724–732.

14. Wilkinson, M.J., Manoogian, E.N.C., Zadourian, A., Lo, H., Fakhouri, S., Shoghi, A., Wang, X., Fleischer, J.G., Navlakha, S., Panda, S., and Taub, P.R. (2020). Ten-hour time-restricted eating reduces weight, blood pressure, and atherogenic lipids in patients with metabolic syndrome. Cell Metab. *31*, 92–104.e5.

15. Cienfuegos, S., Gabel, K., Kalam, F., Ezpeleta, M., Wiseman, E., Pavlou, V., Lin, S., Oliveira, M.L., and Varady, K.A. (2020). Effects of 4- and 6-h time-restricted feeding on weight and cardiometabolic health: a randomized controlled trial in adults with obesity. Cell Metab. *32*, 366–378.e3.

16. Livelo, C., Guo, Y., and Melkani, G.C. (2022). A skeletal muscle-centric view on time-restricted feeding and obesity under various metabolic challenges in humans and animals. Int. J. Mol. Sci. *24*, 422.

17. Schönfeld, P., and Reiser, G. (2017). Brain energy metabolism spurns fatty acids as fuel due to their inherent mitotoxicity and potential capacity to unleash neurodegeneration. Neurochem. Int. *109*, 68–77.

18. Horton, J.L., Davidson, M.T., Kurishima, C., Vega, R.B., Powers, J.C., Matsuura, T.R., Petucci, C., Lewandowski, E.D., Crawford, P.A., Muoio, D.M., et al. (2019). The failing heart utilizes 3-hydroxybutyrate as a metabolic stress defense. JCI Insight *4*, e124079.

19. Aubert, G., Martin, O.J., Horton, J.L., Lai, L., Vega, R.B., Leone, T.C., Koves, T., Gardell, S.J., Krüger, M., Hoppel, C.L., et al. (2016). The failing heart relies on ketone bodies as a fuel. Circulation *133*, 698–705.

20. Karagiannis, F., Peukert, K., Surace, L., Michla, M., Nikolka, F., Fox, M., Weiss, P., Feuerborn, C., Maier, P., Schulz, S., et al. (2022). Impaired ketogenesis ties metabolism to T cell dysfunction in COVID-19. Nature *609*, 801–807.

21. Dmitrieva-Posocco, O., Wong, A.C., Lundgren, P., Golos, A.M., Descamps, H.C., Dohnalová, L., Cramer, Z., Tian, Y., Yueh, B., Eskiocak, O., et al. (2022). beta-Hydroxybutyrate suppresses colorectal cancer. Nature *605*, 160–165.

22. Garza-González, S., Nieblas, B., Solbes-Gochicoa, M.M., Altamirano, J., and García, N. (2022). Intermittent fasting as possible treatment for heart failure. Curr. Vasc. Pharmacol. *20*, 260–271.

23. Kitaura, T., Tsunekawa, N., and Hatta, H. (2001). Decreased monocarboxylate transporter 1 in rat soleus and EDL muscles exposed to clenbuterol. J. Appl. Physiol. *91*, 85–90.

24. Koves, T.R., Zhang, G.F., Davidson, M.T., Chaves, A.B., Crown, S.B., Johnson, J.M., Slentz, D.H., Grimsrud, P.A., and Muoio, D.M. (2023). Pyruvate-supported flux through medium-chain ketothiolase promotes mitochondrial lipid tolerance in cardiac and skeletal muscles. Cell Metab. *35*, 1038–1056.e8.

25. Ritterhoff, J., Young, S., Villet, O., Shao, D., Neto, F.C., Bettcher, L.F., Hsu, Y.W.A., Kolwicz, S.C., Jr., Raftery, D., and Tian, R. (2020). Metabolic remodeling promotes cardiac hypertrophy by directing glucose to aspartate biosynthesis. Circ. Res. *126*, 182–196.

26. Messer, J.I., Jackman, M.R., and Willis, W.T. (2004). Pyruvate and citric acid cycle carbon requirements in isolated skeletal muscle mitochondria. Am. J. Physiol. Cell Physiol. *286*, C565–C572.

27. Glancy, B., Barstow, T., and Willis, W.T. (2008). Linear relation between time constant of oxygen uptake kinetics, total creatine, and mitochondrial content in vitro. Am. J. Physiol. Cell Physiol. *294*, C79–C87.

28. Livelo, C., Guo, Y., Abou Daya, F., Rajasekaran, V., Varshney, S., Le, H.D., Barnes, S., Panda, S., and Melkani, G.C. (2023). Time-restricted feeding promotes muscle function through purine cycle and AMPK signaling in Drosophila obesity models. Nat. Commun. *14*, 949.

29. Villanueva, J.E., Livelo, C., Trujillo, A.S., Chandran, S., Woodworth, B., Andrade, L., Le, H.D., Manor, U., Panda, S., and Melkani, G.C. (2019). Time-restricted feeding restores muscle function in Drosophila models of obesity and circadian-rhythm disruption. Nat. Commun. *10*, 2700.

30. Koves, T.R., Ussher, J.R., Noland, R.C., Slentz, D., Mosedale, M., Ilkayeva, O., Bain, J., Stevens, R., Dyck, J.R.B., Newgard, C.B., et al. (2008). Mitochondrial overload and incomplete fatty acid oxidation contribute to skeletal muscle insulin resistance. Cell Metab. *7*, 45–56.

31. Seiler, S.E., Koves, T.R., Gooding, J.R., Wong, K.E., Stevens, R.D., Ilkayeva, O.R., Wittmann, A.H., DeBalsi, K.L., Davies, M.N., Lindeboom, L., et al. (2015). Carnitine acetyltransferase mitigates metabolic inertia and muscle fatigue during exercise. Cell Metab. *22*, 65–76.

32. Muoio, D.M. (2014). Metabolic inflexibility: when mitochondrial indecision leads to metabolic gridlock. Cell *159*, 1253–1262.

33. Muoio, D.M., Noland, R.C., Kovalik, J.P., Seiler, S.E., Davies, M.N., DeBalsi, K.L., Ilkayeva, O.R., Stevens, R.D., Kheterpal, I., Zhang, J., et al. (2012). Muscle-specific deletion of carnitine acetyltransferase compromises glucose tolerance and metabolic flexibility. Cell Metab. *15*, 764–777.

34. Muoio, D.M., and Neufer, P.D. (2012). Lipid-induced mitochondrial stress and insulin action in muscle. Cell Metab. *15*, 595–605.

35. Veech, R.L., Chance, B., Kashiwaya, Y., Lardy, H.A., and Cahill, G.F., Jr. (2001). Ketone bodies, potential therapeutic uses. IUBMB Life *51*, 241–247.

36. Kashiwaya, Y., King, M.T., and Veech, R.L. (1997). Substrate signaling by insulin: a ketone bodies ratio mimics insulin action in heart. Am. J. Cardiol. *80*, 50A–64A.

37. Al Batran, R., Gopal, K., Capozzi, M.E., Chahade, J.J., Saleme, B., Tabatabaei-Dakhili, S.A., Greenwell, A.A., Niu, J., Almutairi, M., Byrne, N.J., et al. (2020). Pimozide alleviates hyperglycemia in diet-induced obesity by inhibiting skeletal muscle ketone oxidation. Cell Metab. *31*, 909–919.e8.

38. Stagg, D.B., Gillingham, J.R., Nelson, A.B., Lengfeld, J.E., d'Avignon, D.A., Puchalska, P., and Crawford, P.A. (2021). Diminished ketone interconversion, hepatic TCA cycle flux, and glucose production in D-beta-hydroxybutyrate dehydrogenase hepatocyte-deficient mice. Mol. Metab. *53*, 101269.

39. Williams, A.S., Koves, T.R., Pettway, Y.D., Draper, J.A., Slentz, D.H., Grimsrud, P.A., Ilkayeva, O.R., and Muoio, D.M. (2022). Nicotinamide riboside supplementation confers marginal metabolic benefits in obese mice without remodeling the muscle acetyl-proteome. iScience *25*, 103635.

40. Mina, A.I., LeClair, R.A., LeClair, K.B., Cohen, D.E., Lantier, L., and Banks, A.S. (2018). CalR: a web-based analysis tool for indirect calorimetry experiments. Cell Metab. *28*, 656–666.e1.

41. Li, Q., Deng, S., Ibarra, R.A., Anderson, V.E., Brunengraber, H., and Zhang, G.F. (2015). Multiple mass isotopomer tracing of acetyl-CoA metabolism in Langendorff-perfused rat hearts: channeling of acetyl-CoA from pyruvate dehydrogenase to carnitine acetyltransferase. J. Biol. Chem. *290*, 8121–8132.

42. He, W., Berthiaume, J.M., Previs, S., Kasumov, T., and Zhang, G.F. (2023). Ischemia promotes acyl-CoAs dephosphorylation and propionyl-CoA accumulation. Metabolomics *19*, 12.

43. Puchalska, P., Martin, S.E., Huang, X., Lengfeld, J.E., Daniel, B., Graham, M.J., Han, X., Nagy, L., Patti, G.J., and Crawford, P.A. (2019). Hepatocyte-macrophage acetoacetate shuttle protects against tissue fibrosis. Cell Metab. *29*, 383–398.e7.

44. DeBalsi, K.L., Wong, K.E., Koves, T.R., Slentz, D.H., Seiler, S.E., Wittmann, A.H., Ilkayeva, O.R., Stevens, R.D., Perry, C.G.R., Lark, D.S., et al. (2014). Targeted metabolomics connects thioredoxin-interacting protein (TXNIP) to mitochondrial fuel selection and regulation of specific oxidoreductase enzymes in skeletal muscle. J. Biol. Chem. *289*, 8106–8120.

45. Millington, D.S., and Stevens, R.D. (2011). Acylcarnitines: analysis in plasma and whole blood using tandem mass spectrometry. Methods Mol. Biol. *708*, 55–72.

46. Ahn, W.S., and Antoniewicz, M.R. (2011). Metabolic flux analysis of CHO cells at growth and non-growth phases using isotopic tracers and mass spectrometry. Metab. Eng. *13*, 598–609.

47. Antoniewicz, M.R., Kelleher, J.K., and Stephanopoulos, G. (2007). Accurate assessment of amino acid mass isotopomer distributions for metabolic flux analysis. Anal. Chem. *79*, 7554–7559.

48. Fernandez, C.A., Des Rosiers, C., Previs, S.F., David, F., and Brunengraber, H. (1996). Correction of 13C mass isotopomer distributions for natural stable isotope abundance. J. Mass Spectrom. *31*, 255–262.

49. Wang, Y., Christopher, B.A., Wilson, K.A., Muoio, D., McGarrah, R.W., Brunengraber, H., and Zhang, G.F. (2018). Propionate-induced changes in cardiac metabolism, notably CoA trapping, are not altered by l-carnitine. Am. J. Physiol. Endocrinol. Metab. *315*, E622–E633.

50. Tomcik, K., Ibarra, R.A., Sadhukhan, S., Han, Y., Tochtrop, G.P., and Zhang, G.F. (2011). Isotopomer enrichment assay for very short chain fatty acids and its metabolic applications. Anal. Biochem. *410*, 110–117.

51. Li, Q., Zhang, S., Berthiaume, J.M., Simons, B., and Zhang, G.F. (2014). Novel approach in LC-MS/MS using MRM to generate a full profile of acyl-CoAs: discovery of acyl-dephospho-CoAs. J. Lipid Res. *55*, 592–602.

52. Zhang, G.F., Kombu, R.S., Kasumov, T., Han, Y., Sadhukhan, S., Zhang, J., Sayre, L.M., Ray, D., Gibson, K.M., Anderson, V.A., et al. (2009). Catabolism of 4-hydroxyacids and 4-hydroxynonenal via 4-hydroxy-4-phosphoacyl-CoAs. J. Biol. Chem. *284*, 33521–33534.

53. Coleman, T.M., Li, N., and Huang, F. (2005). A simple and efficient method to prepare thioesters in aqueous solutions. Tetrahedron Lett. *46*, 4307–4310.

54. Fisher-Wellman, K.H., Davidson, M.T., Narowski, T.M., Lin, C.T., Koves, T.R., and Muoio, D.M. (2018). Mitochondrial diagnostics: a multiplexed assay platform for comprehensive assessment of mitochondrial energy fluxes. Cell Rep. *24*, 3593–3606.e10.

55. Wilson, R.J., Lyons, S.P., Koves, T.R., Bryson, V.G., Zhang, H., Li, T., Crown, S.B., Ding, J.D., Grimsrud, P.A., Rosenberg, P.B., and Muoio, D.M. (2022). Disruption of STIM1-mediated Ca(2+) sensing and energy metabolism in adult skeletal muscle compromises exercise tolerance, proteostasis, and lean mass. Mol. Metab. *57*, 101429.

56. Koves, T.R., Zhang, G.F., Davidson, M.T., Chaves, A.B., Crown, S.B., Johnson, J.M., Slentz, D.H., Grimsrud, P.A., and Muoio, D.M. (2023). Pyruvate-supported flux through medium-chain ketothiolase promotes mitochondrial lipid tolerance in cardiac and skeletal muscles. Cell Metab. *35*, 1038–1056.e8.

57. Lyons, S.P., Wilson, R.J., Muoio, D.M., and Grimsrud, P.A. (2022). Proteomics and phosphoproteomics datasets of a muscle-specific STIM1 loss-of-function mouse model. Data Brief *42*, 108051.

58. Chambers, M.C., Maclean, B., Burke, R., Amodei, D., Ruderman, D.L., Neumann, S., Gatto, L., Fischer, B., Pratt, B., Egertson, J., et al. (2012). A cross-platform toolkit for mass spectrometry and proteomics. Nat. Biotechnol. *30*, 918–920.

59. Kong, A.T., Leprevost, F.V., Avtonomov, D.M., Mellacheruvu, D., and Nesvizhskii, A.I. (2017). MSFragger: ultrafast and comprehensive peptide identification in mass spectrometry-based proteomics. Nat. Methods *14*, 513–520.

60. da Veiga Leprevost, F., Haynes, S.E., Avtonomov, D.M., Chang, H.Y., Shanmugam, A.K., Mellacheruvu, D., Kong, A.T., and Nesvizhskii, A.I. (2020). Philosopher: a versatile toolkit for shotgun proteomics data analysis. Nat. Methods *17*, 869–870.

61. Yu, F., Haynes, S.E., and Nesvizhskii, A.I. (2021). IonQuant enables accurate and sensitive label-free quantification with FDR-controlled match-between-runs. Mol. Cell Proteomics *20*, 100077.

62. Kohler, D., Staniak, M., Tsai, T.H., Huang, T., Shulman, N., Bernhardt, O.M., MacLean, B.X., Nesvizhskii, A.I., Reiter, L., Sabido, E., et al. (2023). MSstats version 4.0: statistical analyses of quantitative mass spectrometry-based proteomic experiments with chromatography-based quantification at scale. J. Proteome Res. *22*, 1466–1482.

63. Huang, T., Choi, M., Tzouros, M., Golling, S., Pandya, N.J., Banfai, B., Dunkley, T., and Vitek, O. (2020). MSstatsTMT: statistical detection of differentially abundant proteins in experiments with isobaric labeling and multiple mixtures. Mol. Cell. Proteomics *19*, 1706–1723.

64. Ulgen, E., Ozisik, O., and Sezerman, O.U. (2019). pathfindR: an R package for comprehensive identification of enriched pathways in omics data through active subnetworks. Front. Genet. *10*, 858.

STAR★METHODS

KEY RESOURCES TABLE

REAGENT or RESOURCE	SOURCE	IDENTIFIER
Antibodies		
PDHE1a (S293)	Calbiochem	Cat#: AP1062; RRID: AB_10616069
Total PDHE1a	Abcam	Cat#: ab110330; RRID: AB_10858459
MKT (Acaa2)	Millipore Sigma	Cat#: WH0010449M1; RRID: AB_2219394
BDH1	ProteinTech	Cat#: 15417-1-AP; RRID: AB_2274683
SCOT	ProteinTech	Cat#: 12175-1-AP; RRID: AB_2157444
ATP5a	Abcam	Cat#: ab14748; RRID: AB_301447
ACAT1	BioRad	Cat#: VMA00962; RRID: AB_3083664
Chemicals, peptides, and recombinant proteins		
Ethyl [U-^{13}C]acetoacetate	Cambridge Isotope Laboratories	Cat#: CLM-3297; CAS#: 84508-55-4
[U-^{13}C]3OHB	Cambridge Isotope Laboratories	Cat#: CLM-3853; CAS#: 2483735-72-2
[U-^{13}C]palmitic acid	Cambridge Isotope Laboratories	Cat#: CLM-6059; CAS#: 2483736-17-8
[U-^{13}C]glucose	Cambridge Isotope Laboratories	Cat#: CLM-1396; CAS#: 110187-42-3
Lithium acetoacetate	Millipore Sigma	Cat#: A8509; CAS#: 3843-11-2
Sodium 3OHB	Millipore Sigma	Cat#: 54965; CAS#: 150-83-4
Sodium palmitate	Millipore Sigma	Cat#: P9767; CAS#: 408-35-5
Sodium oleate	Millipore Sigma	Cat#: O3880; CAS#: 143-19-1
Bovine Serum Albumin (Fatty Acid Free)	Millipore Sigma	Cat# A9205; CAS# 9048-46-8
Porcine Insulin	Millipore Sigma	Cat#: I5523; CAS#: 12584-58-6
L-Carnitine HCl	Millipore Sigma	Cat# C0283; CAS# 6645-46-1
Norvaline	Millipore Sigma	Cat# N7627; CAS# 6600-40-4
[$^{2}H_9$]L-carnitine	Cambridge Isotope Laboratories	Cat# DLM-3555; CAS# 126827-79-0
[2,2,3,3,4,4,5,5,5-$^{2}H_9$]pentanoic acid	Millipore Sigma	Cat# 493201; CAS# 115871-50-6
Methylhydroxylamine (MOX)	Millipore Sigma	Cat# 226904; CAS# 593-56-6
MTBSTFA (with 1% t-BDMCS)	Millipore Sigma	Cat# M-108; CAS# 77377-52-7
Methanol	Millipore Sigma	Cat# 439193; CAS# 67-56-1
Chloroform	Millipore Sigma	Cat# C2432; CAS# 67-66-3
Acetonitrile	Fisher Scientific	Cat# A955; CAS# 75-05-8
Ammonium formate	Millipore Sigma	Cat# 516961; CAS# 540-69-2
Acetic acid	Millipore Sigma	Cat# 695092; CAS# 64-19-7
Acidic methanol (3N in HCl)	Millipore Sigma	Cat# 90964; CAS# 7647-01-0
2-2(pyridyl)ethyl-functionalized silica gel	Millipore Sigma	Cat# 537985; CAS# N/A
Pentobarbital (Nembutal)	Oak Pharmaceuticals	N/A
Protease Inhibitor Cocktail	Millipore Sigma	Cat# P8340
Phosphatase Inhibitor Cocktail 2	Millipore Sigma	Cat# P5726
Phosphatase Inhibitor Cocktail 3	Millipore Sigma	Cat# P0044
Pierce Reversible Protein Stain Kit for Nitrocellulose Membranes (Memcode)	ThermoFisher Scientific	Cat# 24580
4-15% Criterion TGX Stain-Free Protein Gel, 18well	BioRad	Cat# 5678084
10X Tris Glycine SDS Running Buffer	BioRad	Cat# 1610732
10X Tris-Buffered Saline	BioRad	Cat# 1706435
Fish Gelatin	Millipore Sigma	Cat# G7765
Casein	Millipore Sigma	Cat# C0626
Sodium Nitrate	Millipore Sigma	Cat# S8032

(*Continued on next page*)

Continued

REAGENT or RESOURCE	SOURCE	IDENTIFIER
Roche cOmplete ULTRA EDTA-free Protease Inhibitor Mini Tablet	Millipore Sigma	Cat# 05892791001
Roche 1x PhosSTOP Phosphatase Inhibitor Cocktail Tablets	Millipore Sigma	Cat# 04906837001
Lysyl Endopeptidase, Mass Spectrometry Grade	Wako Chemicals	Cat# 125-05061
Sequencing Grade Modified Trypsin	Promega	Cat# V5113
tC18 SEP-PAK Solid Phase Extraction Columns (50 mg)	Waters	Cat# WAT054960
tC18 SEP-PAK Solid Phase Extraction Columns (100 mg)	Waters	Cat# WAT036820
Triethylammonium bicarbonate (TEAB)	ThermoFisher	Cat# 90114
TMT10plex Isobaric Label Reagent Set (0.8 mg per tag)	ThermoFisher	Cat# 90110
MyTaq Red 2x Mix	Bioline	Cat# BIO-25044
MOPS Free Acid	Millipore Sigma	Cat# M1254; CAS# 1132-61-2
MES Potassium Salt	Millipore Sigma	Cat# M0895; CAS# 39946-25-3
Bovine Serum Albumin (Fatty Acid Free)	Millipore Sigma	Cat# A3803; CAS# 9048-46-6
EDTA	Millipore Sigma	Cat# E0270; CAS# 65501-24-8
Trypsin from Porcine Pancreas (Mitochondrial Isolation)	Millipore Sigma	Cat# T4799; CAS# 9001-51-8
Potassium Chloride	Millipore Sigma	Cat# P5405; CAS# 7447-40-7
Magnesium Chloride Hexahydrate	Millipore Sigma	Cat# M2670; CAS# 7791-18-6
EGTA	Millipore Sigma	Cat# E4378; CAS# 67-42-5
Potassium Dihydrogen Phosphate	Millipore Sigma	Cat# P9791; CAS# 7778-77-0
Creatine Monohydrate	Millipore Sigma	Cat# C3630; CAS# 6020-87-7
Potassium Salt of Phosphocreatine	Millipore Sigma	N/A
Palmitoyl-L-carnitine	Millipore Sigma	Cat# P1645; CAS# 18877-64-0
Octanoyl-L-carnitine	Millipore Sigma	Cat# 50892; CAS# 25243-95-2
Malic Acid (Malate)	Millipore Sigma	Cat# M1000; CAS# 97-67-6
Potassium Pyruvate	Combi-Blocks	Cat# QA-1116; CAS# 4151-33-1
Creatine Kinase from Rabbit Muscle	Roche	Cat# 10127566001
Tetramethylrhodamine Methyl Ester (TMRM)	ThermoFisher	Cat# T668
Rotenone	Millipore Sigma	Cat# R8875; CAS# 83-79-4
Potassium Cyanide	Millipore Sigma	Cat# 60178; CAS# 151-50-8
Alamethicin	AG Scientific	A-1286; CAS#27061-78-5
CDNB	Millipore Sigma	Cat# 237329; CAS# 97-00-7
Critical commercial assays		
Pierce Quantitative Colorimetric Peptide Assay	ThermoFisher	Cat# 23275
Pierce BCA Protein Assay	ThermoFisher	Cat# 23225
ALPCO STELLUX Chemi Rodent ELISA Kit	ALPCO	Cat# 80-INSMR-CH01
FUJIFILM Wako HR Series NEFA-HR Reagent Assay – Color Reagent A	FUJIFILM Medical Systems	Cat# 999-34691
FUJIFILM Wako HR Series NEFA-HR Reagent Assay – Color Reagent B	FUJIFILM Medical Systems	Cat# 991-34891
FUJIFILM Wako HR Series NEFA-HR Reagent Assay – Solvent A	FUJIFILM Medical Systems	Cat# 995-34791
FUJIFILM Wako HR Series NEFA-HR Reagent Assay – Solvent B	FUJIFILM Medical Systems	Cat# 993-35191
Deposited data		
Proteomics Raw Data Files	This Publication	ProteomeXchange: PXD047114
Data S1 (Excel File)	This Publication	N/A

(*Continued on next page*)

Continued

REAGENT or RESOURCE	SOURCE	IDENTIFIER
Experimental models: Organisms/strains		
C57BL/6NJ mice	The Jackson Laboratory	Stock# 005304
BDH1 Skeletal Muscle and Heart Specific Knock-Out Mice	The Jackson Laboratory: Ckmm-cre transgene	Tg(Ckmm-cre)5Khn/0 [MGI:2182095]
	Dr. Dan Kelly: BDH1 floxed allele	Bdh1tm1a(EUCOMM)Wtsi [MGI:4432883]
Oligonucleotides		
BDH1 Genotyping Primers (Bdh1-Fwd): 5′-TGC AGG AAT CAG TGC TCT CTC CTA G-3′	IDT	N/A
BDH1 Genotyping Primers (Bdh1-Rev): 5′-GGT GTC AGG GCT GAA GGA TG-3′	IDT	N/A
Cre Genotyping Primers (Cre26-Fwd): 5′-CCT GGA AAA TGC TTC TGT CCG-3′	IDT	N/A
Cre Genotyping Primers (Cre36-Rev): 5′-CAG GGT GTT ATA AGC AAT CCC-3′	IDT	N/A
Cre Genotyping Primers (Spect a2 8514 P3-Fwd): 5′-TAC ATA GAG AAT GGC CAG TCT TTT GAC-3′	IDT	N/A
Cre Genotyping Primers (Spect a2 8514 P4-Rev): 5′-GCA CAA CTG GGT AAG GTT CCT ATT CC-3′	IDT	N/A
Software and algorithms		
Mass Hunter B.07.00	Agilent Technologies	N/A
Analyst v. 1.6.3	Sciex	N/A
MATLAB R2018b	Mathworks	N/A
Proteome Discoverer 2.5	ThermoFisher	N/A
Proteomics Statistical Analysis	This publication	https://zenodo.org/records/10553167
DatLab 7	Oroboros Instruments	Product# 20700
CalR	Mina et al.[40]	https://calrapp.org
Other		
80x MULTIVAP Nitrogen Evaporator	Organomation	Cat# 11880
Agilent Gas Chromatographer	Agilent Technologies	Cat# 7890B GC
Agilent Mass Spectrometer	Agilent Technologies	Cat# 5977A MSD
Agilent HP-5ms Column	Agilent Technologies	Cat# 19091S-433UI
Sciex LC-MS	Sciex	Cat# Exion AD LC System with QTRAP 6500+ MS/MS
Pursuit XRs C18 Column	Agilent Technologies	Cat# A6000150X020
Zorbax 300StableBond C8 Column	Agilent Technologies	Cat# 861775-906
Tissue Lyser II	Qiagen	Cat# 85300
Heart perfusion system (Langendorff)	Radnoti	Cat# 130102EZ
Mouse diet (10% kcal as fat and 17% kcal as sucrose)	Research Diets	Cat# D12450Hi
EDTA-coated capillary tubes MICROVETTE CB300	Sarstedt	Cat# 16.444.100
Exer-3/6 treadmill	Columbus Instruments	Cat# 1050-RM
Oxygraph-2k	Oroboros Instruments	Cat# O2k-Core
QuantaMaster Spectrofluorometer	Horiba Scientific	Cat# QM-400
Spectrosil Quartz Cuvettes	Starna	23–5.45-Q-5
Spectromax M2E Spectrophotometer	Molecular Devices	Part#: M2E
Thermo Scientific LTQ Orbitrap XLTM Mass Spectrometer	ThermoScientific	Cat#: 0726030
Thermo Fisher Scientific nanoEASY nLC	ThermoScientific	Cat #: LC140
Waters Xevo TQ-S triple quadrupole mass spectrometer coupled to a Waters Acquity UPLC system	Waters	Part#: Xevo TQ-S
Bio-Rad Turboblot Transfer System	Biorad	Cat# 1704150EDU

RESOURCE AVAILABILITY

Lead contact

Further information and requests for resources and reagents should be directed to and will be fulfilled by the lead contact, Deborah Muoio, PhD (muoio@duke.edu).

Materials availability

All unique/stable reagents generated in this study are available from the lead contact with a completed Materials Transfer Agreement.

Data and code availability

- Original western blot images and a file with all data presented in figures are included in Data S4. The proteomics raw data has been submitted to ProteomeXchange (PXD047114) and jPOST (JPST002394) using the indicated accession numbers.
- Original code was generated for proteomic data analysis and is available through the DOI listed in the key resources table.
- Any additional information required to reanalyze the data reported in this paper is available from the lead contact upon request.

EXPERIMENTAL MODEL AND SUBJECT DETAILS

Animal studies

All animal studies were approved by the Duke University Institutional Animal Care and Use Committee (IACUC) and conducted in Association for Assessment and Accreditation of Laboratory Animal Care (AALAC) accredited facilities. Male mice on a C57BL/6NJ background from Jackson Laboratory (strain #005304) were used for all experiments in Figure S1. Figure 1. For all experiments with BDH1^{MCK} (mKO) mice, BDH1$^{fl/fl}$ mice on a C57BL/6NJ background were generated as described in Horton et al.[18] and crossed with muscle creatine kinase (MCK)-Cre transgenic mice to generate mice with a skeletal muscle and heart-specific deletion of BDH1 (BDH1^{MCK} or mKO mice) and littermate controls (BDH1$^{fl/fl}$ or FC) mice. Male mice were used for all experiments and were housed in a light (12h light/12h dark) and temperature (22°C) controlled room and had *ad libitum* access to food and water unless noted otherwise. The TRF experimental designs are summarized in Figures 1A and 5A. Briefly, mice were fed a standard chow diet (Lab Diet PicoLab Rodent Diet 20 5053) and allowed to acclimate to the animal facility for approximately one week. Next, mice were placed in cages with alpha-dri bedding, fed a standard chow diet and transferred to a light (12h light/12h dark) and temperature (22°C) controlled environmental cabinet (Powers Scientific) with a shifted light/dark cycle (12p.m. (on) and 12a.m. (off)). Mice were allowed to acclimate to the cabinet for 2–3 weeks and pre-special diet phenotyping (noted as pre-diet) was conducted then mice were switched to a special diet (10% kcal as fat and 17% kcal as sucrose, Research Diets D12450Hi) for an additional two weeks. At 12–14 weeks of age, all mice underwent post-special diet phenotyping (noted as Pre in Figures 1A and 5A and post-diet in Figures 1D, 1F, and 5D–5F) that included measures of body composition in the fed state and body mass, blood glucose and blood beta-hydroxybutyrate (3OHB) in the fed (ZT 3) and 18h fasted (ZT 21) states. Mice were then assigned to one of two groups: *ad libitum* (Ad Lib) or intermittent time-restricted feeding (TRF). TRF mice were allowed *ad libitum* access to food for 6h per day (e.g., 18h fast and 6h feed or 18:6) during zeitgeber time (ZT) 21-3 for 4 days a week (Monday - Friday) and were allowed *ad libitum* access to food on days 5–7. During the fasting period, TRF mice were switched into a clean cage with alpha dri bedding and back into their original feeding cage for the 6h feed. All cages were changed at least 2 times per week. Body mass, blood glucose and blood 3OHB were measured weekly at ZT 3 and 21 starting at TRF weeks 1 or 2. Daily food consumption per cage was measured starting at TRF week 4. For experiments in C57BL/6NJ mice, all mice underwent an acute fasting challenge (AFC) at TRF week 8 and for experiments in BDH1 mKO and FC mice all mice underwent an AFC at the following timepoints: pre-diet, 2 weeks post-special diet (post-diet) and TRF weeks 4 and 11. The experimental design for all AFCs is shown in Figure S1. Briefly, body mass, body composition, blood metabolites (glucose and 3OHB), and tail blood samples were obtained from ad lib and TRF mice in the fed, 18h fasted (fast), and 6h refed states (refed). Food consumption per cage was determined during the 6h refeed period.

METHOD DETAILS

Chemicals and reagents

All chemicals were purchased from Sigma-Aldrich unless otherwise stated. Creatine kinase from rabbit muscle was purchased from Roche Life Science Publishing. Tetramethylrhodamine methyl ester (TMRM) and Amplex Ultra Red were purchased from Thermo Fisher Scientific. Potassium pyruvate was purchased from Combi-Blocks. All tracers were purchased from Cambridge Isotope Laboratories.

Blood and plasma metabolites

Blood glucose was determined as previously described.[39] Blood 3OHB was determined using a Keto-Mojo Ketone Meter (Keto-Mojo). Tail blood was collected using EDTA-coated capillary tubes (Sarstedt MICROVETTE CB300, Sarstedt) and plasma was isolated for the determination of non-esterified free fatty acids (NEFAs) using the FUJIFILM Wako HR Series NEFA-HR reagent assay

(FUJIFILM Medical Systems) according to manufacturer's instructions with the following modifications: fed and 6h refed samples were diluted 1:2 in 0.9% saline and 18h fasted samples were diluted 1:4 in 0.9% saline.

Body composition and energy balance

Body mass was monitored weekly or bi-weekly. Body composition and indirect calorimetry were determined via CLAMS as previously described.[39] For the CLAMS study, TRF mice were fed at ZT 21 and allowed 2h *ad libitum* access to food. Next, Ad Lib and TRF mice were weighed and placed in metabolic cages without food and the CLAMS run was started. Mice remained in the CLAMS for approximately 19h without food and a pre-weighed portion of food was added to each cage. After 6h, the CLAMS run was stopped and mice and food were weighed. Raw data were uploaded into CalR for data analysis and visualization (https://calrapp.org).[40]

Glucose homeostasis

Mice were group housed and fasted on alpha-dri bedding with access to water. Measures of glucose homeostasis were assessed as previously described[39]) with the following modifications. Glucose homeostasis was determined under two different nutritional conditions: 1) Friday (TRF day 5) - TRF mice were pair fed to ad lib controls for 3h and all mice were then fasted for 2h and 2) Monday (TRF day 1) after both ad lib and TRF mice were allowed to feed *ad libitum* for 72h - Ad Lib and TRF mice were fasted for 5h. For OGTTs, mice were gavaged with a 1.5 g/kg lean mass glucose solution.

Exercise tolerance

Exercise time and distance to fatigue were determined using a graded exercise challenge in 18h fasted mice. Mice were habituated to an open-air Exer-3/6 treadmill equipped with a shock grid (Columbus Instruments) for 3 days. The treadmill was set to a fixed incline of 10% and the exercise bout was initiated at a speed of 10 m/min for 30 min. The speed was increased to 2 m/min every 15 min, and then once the speed reached 28 m/min the speed was increased by 2 m/min every 10 min until exhaustion.

iTRF mouse harvests

For data in Figure S1. Figure 1, TRF mice were subjected to a continuous TRF regimen for at least 2 weeks and Ad lib and TRF mice were fasted for 12h with access to water before harvest. For data in Figures S4–S6, 4, 5, and 6, TRF mice were allowed to feed *ad libitum* for 72h and TRF and Ad lib mice were fasted for 5h with access to water before harvest. At harvest, mice were anesthetized with Nembutal (10 mg/kg body weight) and tissues were excised.

Langendorff heart perfusions

Overnight fasted (~18-20h), 22-week-old, BDH1 mKO and FC mice were anesthetized with isoflurane. Next, a median laparotomy was performed[41,42] and a bolus of heparin (500U/kg) was given via the inferior vena cava. An incision in the diaphragm was made and the thorax was filled with 100 mL of ice-cold Krebs-Ringer bicarbonate buffer to initiate cardioplegia. The heart was quickly excised and immersed in ice-cold Krebs–Ringer buffer until complete cardioplegia. The aortic arch was carefully dissected and cannulated with a 25-gauge cannula attached to a modified Langendorff apparatus. The hearts were perfused in retrograde fashion (Langendorff) with gassed (95% O_2, 5% CO_2) modified Krebs-Ringer bicarbonate buffer (pH 7.4) containing 119mM NaCl, 4.8mM KCl, 2.6mM $CaCl_2$, 1.2mM KH_2PO_4, 1.2mM $MgSO_4$, 25 mM $NaHCO_3$, 11mM glucose, and 0.05mM carnitine.[41] Perfusate was delivered at continuous flow (1.2 mL/min) with a RAININRabbit-Plus peristaltic pump (Woburn, MA, USA) in nonrecirculating mode. A water-jacketed chamber was used to maintain temperature. The perfusion medium was passed through a Radnoti glass bubble trap before entering the heart cannula to ensure no bubbles entered the heart and the heart was held at a constant temperature of 37°C. The hearts were perfused with Krebs-Ringer bicarbonate buffer for 5 min and then switched to perfusate containing the labeled substrates (1 mM [$^{13}C_{16}$] palmitate, 5 mM glucose, 1 mM 3OHB, and 0.33 mM AcAc) for 30 min. The hearts were allowed to beat spontaneously throughout the perfusion. At the end of each perfusion, hearts were snap-frozen in liquid nitrogen and stored at −80°C until further analysis.[42]

Isolated skeletal muscle incubations

Sodium [U-^{13}C]AcAc was synthesized from ethyl [U-^{13}C]AcAc by base-catalyzed hydrolysis as previously described[43] and quantified by GC-MS isotope dilution technique. Mouse soleus (SOL) and EDL muscles (SkM) were excised and incubated in a base buffer as described.[44] SkM were exposed to three separate buffers: (1) excision buffer at room temperature; (2) equilibration buffer at 29°C for 15′ and then 37°C for 15′ and (3) ^{13}C-tracer buffer at 37°C for 90'. The excision/equilibration buffers were 5mM glucose +0.5% BSA unless noted otherwise. After tracer incubation, SkM were rinsed in ice-cold KHB +0.5% BSA and flash frozen. SkM and buffers were stored at −80°C until processed.

Experiment 1 (Figures S2 and 2)

SkM from Ad Lib fed or 16h fasted, 16-week-old, WT mice were incubated in either a fasted or fed buffer. The fasted excision/equilibration buffer was 3mM glucose +0.5% BSA and the tracer buffer was 3mM glucose +1.5mM oleate:palmitate (1:1) + 2.1% BSA +0.75mM [U-^{13}C]3OHB +0.25mM AcAc. The fed equilibration buffer was 7mM glucose +0.5% BSA and the tracer buffer was 7mM glucose +0.5mM oleate:palmitate (1:1) + 0.7% BSA +0.1mM [U-^{13}C]3OHB +0.1mM AcAc +100nM insulin.

Experiment 2 (Figures S3 and 3)

SkM from 12 or 18h fasted, 37-47-week-old, BDH1 mKO and FC mice were incubated in fasted buffer. Tracing studies were performed in parallel, wherein SkM were incubated with identical substrate conditions and only the ^{13}C-tracer differed. The tracing buffers were 5mM glucose + 1mM palmitate +1.4% BSA +0.75mM 3OHB +0.25mM AcAc and one of the following substrates was uniformly ^{13}C-labeled: 3OHB, AcAc, or palmitate.

Experiment 3 (Figure 5)

SkM from 5h fasted, 31–38 week old, TRF and Ad Lib, BDH1 mKO and FC mice were incubated in fed buffer with 10mM [U-^{13}C] glucose +0.2mM palmitate +0.28% BSA +0.1mM 3OHB +0.1mM AcAc + 5nM insulin.

Quantification of 3OHB and AcAc consumption rates

3OHB and AcAc consumption rates were determined by an isotope dilution technique. Briefly, SkM were incubated with [U-^{13}C]AcAc in either fasted or fed buffer and spent buffer was collected in two 100uL aliquots: (1) spiked with [U-^{13}C]3OHB (0.25mM - fast; 0.1mM - fed) and [U-^{12}C]AcAc (0.25mM - fast; 0.1mM - fed) at equal volume ratio or (2) no spike. Proteins were precipitated upon addition of 80% MeOH (4:1, MeOH:buffer), and centrifugation at 4°C and 14400g for 10 min. The aqueous phases were split into two aliquots, dried under nitrogen gas at 37°C (Organomation) and stored at −80°C. After MS analysis, 3OHB and AcAc quantification was performed as follows:

$$MID_{spike} = f * MID_{IS} + (1 - f) * MID_{expt} \quad \text{(Equation 1)}$$

Where MID_{spike} is the mass isotopomer distribution (MID) of the spiked sample, MID_{expt} is the MID of the unspiked sample, MID_{IS} is the MID of the ^{13}C-3OHB/^{12}C-AcAc standard, and f is the molar fraction of the spiked sample that is due to the internal standard. Since the internal standard amount, x_{IS}, is known, regression of the best fit for f allows determination of the analyte moles x_{expt} in the spent buffer by:

$$x_{expt} = x_{IS}\frac{(1 - f)}{f} \quad \text{(Equation 2)}$$

From these values, the rates of 3OHB/AcAc uptake and/or production can be calculated. The external rates around 3OHB and AcAc allow estimation of net BDH1 and SCOT flux. The assumption for these calculations is metabolic steady state, i.e., constant flux and pool size.

$$BDH1_{net} = 3OHB_{uptake} \quad \text{(Equation 3)}$$

$$BDH1_{rev} = M4\ 3OHB_{efflux} \quad \text{(Equation 4)}$$

$$SCOT_{net} = 3OHB_{uptake} + AcAc_{uptake} \quad \text{(Equation 5)}$$

Tissue homogenization and extraction

SkM were homogenized using a Tissue Lyser (Qiagen) via a modified folch extraction method, dried under nitrogen gas at 37°C (Organomation) and stored at −80°C until preparation for MS assays.

GC-MS assay

Both tissue and buffer samples were prepared for GC-MS with MOX and TBDMS as described previously.[45] GC-MS analyses were performed on an Agilent 7890B GC system equipped with an HP-5MS capillary column (30 m, 0.25 mm i.d., 0.25 μm-phase thickness; Agilent J&W Scientific), connected to an Agilent 5977A Mass Spectrometer operating under ionization by electron impact (EI) at 70 eV. Helium flow was maintained at 1 mL/min. The source temperature was maintained at 230°C, the MS quad temperature at 150°C, the interface temperature at 280°C, and the inlet temperature at 250°C. The injection volume was 1 μL and samples were injected in split or splitless mode depending on analyte of interest. For organic and amino acids, the GC oven temperature was held at 80°C for 2 min, increased to 280 °C at 7 °C/min, and held at 280°C for a total run time of 40 min. Mass spectra were recorded in selected ion monitoring (SIM) mode with 4 ms dwell time. Acetoacetate (m/z 188, 11.2′) and 3OHB (m/z 275, 15.4′) was added to the previous SIM method.[46] Mass isotopomer distributions (MIDs) were obtained by integration of ion chromatograms[47] and corrected for natural isotope abundances.[48] Relative pool size estimates were determined by comparing analyte peak areas to norvaline peak area (m/z 288).

LC-MS/MS for acylcarnitine assay

Acylcarnitines in the muscle tissue were methylated and profiled by the modified LC-MS/MS method.[45,49] Briefly, ∼300 μL SkM extracts were spiked with 0.2 nmol [$^{2}H_{9}$]L-carnitine as an internal standard for methylation derivatization. The derivatized samples were analyzed by LC-QTRAP 6500+-MS/MS (Sciex, Concord, Ontario). LC method was developed on a Pursuit XRs C18 150 × 2.0 mM column in a gradient mode with mobile phase A (98% H2O, 2% acetonitrile, and 0.1% formic acid) and mobile phase B (98%

acetonitrile, 2% H2O, and 0.1% formic acid) at 0.4 mL/min. The column was maintained at room temperature. The gradient started with 100% A at first 2 min and was then decreased to 20% A within 11 min. The column was washed by 90% B for 4.5 min and then was re-equilibrated by 100% A for 6 min before next injection. QTRAP 6500+-MS/MS operated under positive ionization mode with the following source settings: turbo-ion-spray source at 600°C under N2 nebulization at 65 p.s.i., N2 heater gas at 55 p.s.i., curtain gas at 35 p.s.i., collision-activated dissociation gas pressure held at high, turbo ion-spray voltage at 5,500 V, declustering potential at 33 V, entrance potential at 10 V, collision energy at 24 V, and collision cell exit potential at 14 V. The Analyst software (version 1.6.3; Sciex) was used for data processing. Q1 (m/z) was scanned from 176 to 490 and m/z of Q3 was selected at 99 for all acylcarnitines except that Q1 and Q3 of l-carnitine were set at m/z 176 and 117, respectively. The labeling of acylcarnitine was corrected from their natural isotope distribution.[48,50] Relative amounts of acylcarnitine species were determined by normalizing analyte peak areas to [$^{2}H_{9}$]L-carnitine peak area.

LC-MS/MS for acyl-CoA assay

Acyl-CoAs were analyzed based on our previously established method.[51,52] A ~100 mg heart tissue sample was spiked with in-house synthesized standard, [2,2,3,3,4,4,5,5,5-$^{2}H_{9}$]pentanoyl-CoA (0.2 nmol)[53] and homogenized in 1 mL of extraction buffer (5% acetic acid in MeOH/H2O 50:50) using Tissue Lyser (Qiagen, Germantown, MD). The supernatant was run on a 1 mL ion exchange cartridge packed with 100 mg of 2-2(pyridyl)ethyl silica gel. The cartridge was pre-activated with 1 mL methanol, and then equilibrated with 1 mL of extraction buffer. The acyl-CoAs trapped on the silica gel cartridge were eluted with (i) 1 mL of a 1:1 mixture of 50 mM ammonium formate (pH 6.3) and methanol, then (ii) 1 mL of a 1:3 mixture of 50 mM ammonium formate (pH 6.3) and methanol, and (iii) 1 mL of methanol. The combined effluent was dried with N2 gas and stored at −80°C until analysis on by LC-QTRAP 6500+-MS/MS (Sciex, Concord, Ontario). The detailed LC-MS/MS method was described in previous work.[51,52]

Terminology: The natural abundance-corrected MID data was used to compute an 'average' representation of ^{13}C-enrichment in each metabolite (average ^{13}C-labeling enrichment or APE) calculated as:

$$APE(\%) = \sum_{i=1}^{n} \frac{i * (M+i)}{n} * 100 \quad \text{(Equation 6)}$$

where n = the number of carbons, and $M + i$ represents the ith mass isotopomer.

Mitochondrial diagnostics

Mitochondria were isolated and mitochondrial respiratory control, membrane potential and NAD(P)H/NAD(P)$^{+}$ redox were determined as previously described.[54]

BDH1 activity assay

BDH1 activity was assessed using 10ug of freshly isolated or frozen mitochondria. The assay buffer was Buffer D[54] supplemented with alamethicin (0.03 mg/ml), rotenone (0.005mM) and NAD^{+} (2mM). Briefly, 200ul of buffer was added to the well of an opaque 96-well plate followed by mitochondria and 400mM R-3-BHB acid. Rates of NADH production from BDH1 were determined by auto-fluorescence (Ex:Em 340/450). Fluorescence values were converted to pmoles of NADH via a NADH standard curve.

Targeted mass spectrometry-based metabolomics

Tissue and plasma acylcarnitines, amino acids or organic acids were determined as previously described.[55]

Western blot analysis

Mitochondrial pellets and frozen tissues were lysed with 2x sample buffer (20 mM Tris-HCl, 4% SDS, 10 mM NaF, 1 mM EDTA, 20% glycerol, pH 6.8) with protease and phosphatase inhibitors. Following lysis 20-40 μgs of mitochondrial or tissue protein was loaded onto a 4–15% gradient gel (BioRad) and subjected to electrophoresis. Proteins were transferred from the gradient gel to a nitrocellulose membrane using a Trans TurboBlot system (BioRad). Following transfer, membranes were stained with reversible total protein stain (Memcode, Thermofisher Scientific, 1858784). Membranes were then imaged to assess total protein levels. Total protein stain was removed with stain eraser (Thermofisher Scientific, 1858786), and membranes were blocked in a fish gelatin blocking solution for 1h at room temperature. After blocking, membranes were incubated in primary antibodies overnight (MKT, Sigma WH0010449M1; BDH1, ProteinTech 15417-1-AP; SCOT 12175-1-AP, ProteinTech; ACAT1, BioRad VMA00962, ATP5a, Abcam ab14748; pPDH S293, Calbiochem AP1062; and total PDHE1a, Abcam ab110330). Following primary incubation, membranes were washed 5 × 5 min in TBST and then incubated with appropriate secondary antibodies. Membranes were then washed 5 × 5 min in TBST, and 1 × 5 min in TBS. Membranes were imaged using an Odyessy Clx system (Licor).

Proteomic sample preparation

Pelleted mitochondria or tissue samples were prepared for proteomic analysis, as described previously for label-free[56] or isobaric tag-(TMT) based[57] quantitation. Briefly, samples were resuspended in ice-cold Lysis Buffer containing 8M urea, salts, and protease inhibitors. Samples were disrupted by a combination of vortexing, freeze/thaw, and sonication. After clarification by centrifugation, protein content was determined via the BCA assay. Equal amounts of protein (25 μg for label free; 300μg of heart mitochondria or

400 μg of SkM for TMT) was reduced (5 mM DTT) and alkylated (15 mM iodoacetamide). Following dilution of the urea 1:5 with 25 mM Tris pH 8.0, Promega trypsin was added at 1:50 w:w and incubated at 32°C overnight. Samples were desalted with tC18 SEP-PAK Solid Phase Extraction (SPE) columns (Waters), eluted, and dried in a speed vac. The heart mitochondrial and SkM samples were labeled with 11-plex Tandem Mass Tag (TMT) reagents (0.8 mg), quenched with 0.8 μm L hydroxylamine, the respective samples for each experiment mixed, and subjected to offline fractionation.[57]

Proteomic data acquisition

Both label-free and isobaric tag-based quantitative *nano*LC-MS/MS analyses were performed on a Q Exactive Plus Orbitrap (Thermo Fisher Scientific) mass spectrometer coupled to an EASY-nLC UPLC system (Thermo) via a nanoelectrospray ionization source. Approximately 1 μg of each sample was injected and trapped (500 bar max pressure) on an Acclaim PepMap (Thermo) 100 trapping column (3 μm, 75 μm × 20 mm) and separated on an Acclaim PepMap (Thermo) RSLC C18 analytical column (2 μm 100 C18, 75 μm × 500 mm column) over a 105 min gradient of solvent A (0.1% FA) to solvent B (90% ACN/0.1% FA)) at 300 nL/min and a column temperature of 55°C. For label-free analysis, MS^1 spectra (precursor ions) were collected at a resolution (r) of 70,000, a target AGC value of 3e6 ions, and a maximum injection time (IT) of 100 ms, and MS^2 spectra (r = 17,500 AGC = $1x10^5$, max IT = 100 ms) were collected by data-dependent acquisition (DDA) using a loop count of 20, an isolation window of 1.2 m/*z*, normalized collision energy of 27, and dynamic exclusion (DE) enabled for 30 s. Different parameters used for isobaric tag-based analysis are noted (MS1: max IT = 60 ms, MS2: r = 35,000, max IT = 60 ms, isolation window = 0.7 m/z, nce = 30). The proteomics raw data has been submitted to ProteomeXchange (PXD047114) and jPOST (JPST002394) using the indicated accession numbers.

Proteomics data analysis

For both SkM and heart mitochondria, raw files were converted to mzML files using MSconvert from proteowizard[58] and analyzed with Fragpipe (V18), using the MSFragger (V 3.5)[59] search engine and Philosopher (V 4.4.0)[60] for downstream processing. The SkM files were processed using the default TMT10 workflow with TMT-Integrator for quantitation, while the unlabeled heart mitochondria samples were analyzed using the LFQ-MBR workflow with IonQuant.[61] The SkM samples were searched with a FASTA file downloaded inFragpipe on 08-18-2022, and the heart mitochondrial samples used a FASTA downloaded on 09-21-2022, both containing reviewed proteins, protein isoforms for the mouse species (UP000000589) along with common contaminants. Postprocessing data analysis was performed in R (4.2.1). Statistical differences between groups were accessed using MSstats (4.4.1)[62] for the unlabeled data and MSstatsTMT (2.4.1)[63] for the TMT labeled data. Custom scripts were used to generate spreadsheets and figures. Figures were generated in R using ggplot2 (3.3.6), ggprism (1.0.3), and ggrepel (0.9.1). Pathway analysis was performed using the R package pathfindR (1.6.4)[64] using gene set lists from MSigDB, mouse, collection C2, subcollection "CP:REACTOME". Heatmaps were generated using the pheatmap package (1.0.12). Scripts used for all analysis will be available on GitHub.

QUANTIFICATION AND STATISTICAL ANALYSIS

Data are presented as means ± SEM. Statistical analyses were preformed using GraphPad Prism 9.0 (GraphPad Software, San Diego, CA) using two-tailed student's t-tests, one or two-way ANOVAs and ANCOVAs. Figures were generated using GraphPad Prism 9.0. The level of significance for all experiments was set at $p \leq 0.05$.